5-2012

Real-time characterization of ultra-thin organic layers via simultaneous spectroscopic ellipsometry and piezoelectric nanogravimetry

Keith B. Rodenhausen Jr.
University of Nebraska-Lincoln, kbrod@engr.unl.edu

Real-time characterization of ultra-thin organic layers via simultaneous spectroscopic ellipsometry and piezoelectric nanogravimetry

By

Keith B. Rodenhausen, Jr.

A THESIS

Presented to the Faculty of

The Graduate College at the University of Nebraska

In Partial Fulfillment of Requirements

For the Degree of Master of Science

Major: Chemical Engineering

Under the Supervision of Professor Mathias Schubert

Lincoln, Nebraska

May, 2012

Real-time characterization of ultra-thin organic layers via simultaneous spectroscopic ellipsometry and piezoelectric nanogravimetry

Keith B. Rodenhausen, Jr., M.S.
University of Nebraska, 2012

Advisor: Mathias Schubert

Analysis techniques are needed to determine the quantity and structure of materials composing an organic layer that is below an optical ultra-thin film limit and in a liquid environment. Neither optical nor acoustical techniques can independently distinguish between thickness and porosity of ultra-thin films due to parameter correlation. A combined optical and acoustical approach yields sufficient information to determine both thickness and porosity. The author describes application of the combinatorial approach to measure single or multiple organic layers when the total layer thickness is small compared to the wavelength of the probing light. The instrumental setup allows for simultaneous *in-situ* spectroscopic ellipsometry and quartz crystal microbalance dynamic measurements, and it is combined with a multiple-inlet fluid control system for different liquid solutions to be introduced during experiments. A virtual separation approach is implemented into an analysis scheme, differentiated by whether or not the organic adsorbate and liquid ambient densities are equal. The analysis scheme requires that the film be assumed transparent and rigid (non-viscoelastic). The author presents and discusses applications of the approach to studies of organic surfactant adsorption, self-assembled monolayer chemisorption, and multiple-layer target DNA sensor preparation and performance testing.

Acknowledgements

I am extremely grateful to many individuals for their assistance and support that made this work possible. First I thank my advisor and mentor, Prof. Mathias Schubert, for the incredible opportunities from which I have benefited. I thank the members of my Ph.D. committee, Prof. Natale Ianno, Prof. Rebecca Lai, Prof. Angela Pannier, and Prof. Ravi Saraf, for lending their time and expertise to me so that I could develop a better thesis. For invaluable technical support and fruitful discussions, I thank Dr. Mark Poggi (Biolin Scientific), Mark Solinsky (The Procter & Gamble Co.), and Dr. Thomas E. Tiwald (J.A. Woollam Co., Inc.). Dr. Eva Bittrich and Dr. Klaus-Jochen Eichhorn were gracious hosts to me during my research in Dresden, Germany.

My colleagues, Prof. Tino Hofmann, Dr. Daniel Schmidt, Dr. Venkata "Rao" Voora, Dr. Hao Wang, Tadas Kasputis, Jennifer Gerasimov, Alex Boosalis, Eric Montgomery, Stefan Schöche, Philipp Kühne, Dan Liang, Derek Sekora, Chad Briley, and Charles Rice provided me with practical help in the laboratory and enhanced the interdisciplinary nature of this work. Evenings at Yia Yia's and Saturdays at Memorial Stadium will not soon be forgotten.

Financial support for this work was provided by The Procter & Gamble Company, The J.A. Woollam Company, Inc., the National Science Foundation under award number EPS-1004094, and the University of Nebraska-Lincoln College of Engineering.

Finally, I thank my parents, Keith and Kim Rodenhausen, for their love and support and for cultivating a love for science in our family.

Contents

List of Figures

List of Tables

Chapter 1

Introduction

Organic layers of few-nm thickness are important for chemical and biological detection,[1] tissue scaffolding,[2] detergent,[3] and surface property tuning[4] applications. Both qualitative and quantitative understanding of organic adsorbate attachment to solid surfaces is of high contemporary interest, especially if performed within liquid ambient. Porosity is a measure of the solvent content of the layer that has formed onto the solid surface and may be used in further analysis of surface coverage and structural conformation of the organic layer. Measurement of the porosity of an organic layer in a liquid environment is a challenge, particularly if the physical thickness of the layer is on the order of a few nm. *In-situ* instrumentation and analysis methods are needed to effectively monitor organic layers as they attach, detach, or change conformational structure in their liquid environments. Optical and acoustical methods, such as spectroscopic ellipsometry and piezoelectric surface resonance techniques, respectively, are widely employed for non-invasive, contactless, *in-situ* monitoring of organic layer formation. However, for optical ultra-thin organic layers, neither optical nor acoustical techniques can separate between porosity and thickness independently. The optical ultra-thin film limit is met when the total thickness of the organic layer is less than a certain, small fraction of the probing wavelength. At such small thickness, the organic layer may be considered rigid because it does not reveal sufficient viscoelasticity upon acoustic measurement. As discussed in further detail below, the optical ultra-thin film limit is met when $2\pi nd/\lambda \ll 1$, where d is the thickness of the or-

ganic layer, n its index of refraction, and λ is the wavelength of probing light in a linear polarization-dependent optical experiment. Note that the optical ultra-thin film limit is dependent upon material and instrumentation properties because the limit is specific to a substance measured by a linear polarization-dependent optical experiment. For an experiment performed in the visible/near-infrared spectrum (350 nm to 1000 nm), the optical ultra-thin film limit is on the order of a few nm. Acquiring quantitative porosity information from an experiment can be useful for constructing model scenarios that provide insight into the physical structure of the thin film. Thus, (a) instrumentation sensitive to nm-scale organic film growth with sufficient time resolution to allow for dynamic measurements (each a series of data sets taken at regular intervals, or "time slices" of data) and (b) analysis methods capable of yielding the dynamic thickness and porosity of an organic ultra-thin film are particularly advantageous.

Porosity can be defined by a mass or volume fraction. In this work, the author describes porosity in the form of mass and volume adsorbate fraction parameters $f_{\mathrm{o}}^{\mathrm{m}}$ and $f_{\mathrm{o}}^{\mathrm{V}}$, respectively, which are bound between zero and unity. The porosity of organic thin films affects material properties due to the absence of adsorbate and the contribution of ambient inclusions. A porous organic thin film is considered, in this work, to be completely homogenous or to have a homogenous and random distribution of locally heterogeneous inclusions such that the thin film can be considered isotropic on a scale of, or much larger than, the probing wavelength.

Previous experimental efforts to study the porosity of organic ultra-thin films remained qualitative[5–8] or obtained the film thickness and porosity using additional *ex-situ*[9] or separate *in-situ* measurement instrumentation.[10] Stålgren, Erikkson, and Boschkova;[6] and Macakova, Blomberg, and Claesson;[9] monitored surfactant adsorption with a quartz crystal microbalance (QCM) and an optical technique in parallel but on separate substrates for each instrument. Stålgren, Erikkson, and Boschkova used null ellipsometry as the optical technique while Macakova, Blomberg, and Claesson used optical reflectometry. In their analysis, which included quantitative porosity on mass and volume bases, Macakova, Blomberg, and Claesson assumed the adsorbate thickness during their *in-situ* investigations from a neutron scattering experiment and determined the index

of refraction of the organic layer.[9] Richter and Brisson studied the adsorption of lipid vesicles with a quartz crystal microbalance with dissipation (QCM-D), null ellipsometry, and atomic force microscopy, separately.[8] Swann *et al.* used a dual polarization interferometry (DPI) waveguide setup to measure the thickness and conformation of protein adsorption. Aulin *et al.* used QCM-D and DPI on separate silica surfaces to study polyelectrolyte layer-by-layer adsorption. Domack *et al.* used QCM and ellipsometry on the same substrate to study polymer brush swelling. The authors observed that the thickness of the organic films, which were above the optical ultra-thin film limit, were twice as large measured by the QCM than that measured by ellipsometry, indicative of non-zero porosity.[5] Broch *et al.* reported on combined *in-situ* spectroscopic ellipsometry (SE) and electrochemical quartz crystal microbalance (EQCM) instrumentation to monitor thickness and optical property variation of thin films formed by electrode anodization.[11]

In this work, the author discusses an approach to quantitatively determine the *in-situ* thickness *and* porosity of rigid, transparent, organic ultra-thin films by simultaneous SE and QCM measurements on the same sample.[12] The instrumental technique implements a virtual separation approach, which enables the determination of both porosity and physical thickness of ultra-thin films.[13] Material properties that must be known or assumed are the dry organic adsorbate index of refraction n_{o}, the dry organic adsorbate density ρ_{o}, the ambient index of refraction n_{a}, and the ambient density ρ_{a}. SE and QCM allow for the simultaneous acquisition of dynamic measurements that incorporate many individual time slices of experimental data. The time resolution for the dynamic measurements may be adjusted for observation of the kinetic behavior of ultra-thin films and may be limited by instrument capabilities. With a multiple-inlet fluid control system, the liquid ambient over a substrate can be exchanged to introduce adsorbate or begin a non-equilibrium process. The scope of this thesis is to present the overall instrumental approach and its use for monitoring multiple-layered organic ultra-thin film formation.

In Chapter 2, the author discusses the theoretical background for SE, QCM, and the approach for obtaining thickness and porosity parameters for rigid, trans-

parent, organic ultra-thin films. In Chapter 3, the combination of SE and QCM to characterize ultra-thin films and the implementation of the equations derived in Chapter 2 to yield dynamic thickness and porosity are described. In Chapter 4, case studies of surfactant adsorption, alkanethiol self-assembled monolayer (SAM) chemisorption, and target deoxyribonucleic acid (DNA) sequence detection are detailed. The results of these experiments are discussed in Chapter 5.

Chapter 2

Theory

The objective of this chapter is to obtain (a) thickness parameters and (b) porosity in the form of an adsorbate fraction parameter for a rigid, transparent, organic ultra-thin film. The thickness and adsorbate fraction parameters stem from SE and QCM measurement parameters converted from raw instrumental data. In this section, the SE and QCM techniques are described; a virtual separation approach, which demonstrates how SE is not sensitive to ambient inclusions in an ultra-thin film, is discussed; and equations that yield the thickness and adsorbate fraction parameters of an ultra-thin film are provided.

2.1 Spectroscopic ellipsometry

Ellipsometry measures normalized Fourier coefficients that describe the change of polarization state, commonly defined as the complex ratio ϱ, for an electromagnetic wave that reflects off or is transmitted through a sample. A hypothetical experimental setup is shown in Fig. 2.1. Input and output polarizations are described by linearly independent complex amplitudes (e.g., p and s components) of the probing electromagnetic wave, such that [14–16]

$$\varrho = \left(\frac{B_{\zeta'}}{B_{\xi'}}\right) / \left(\frac{A_{\zeta}}{A_{\xi}}\right) = \tan(\Psi) \exp \mathrm{i}\Delta. \tag{2.1}$$

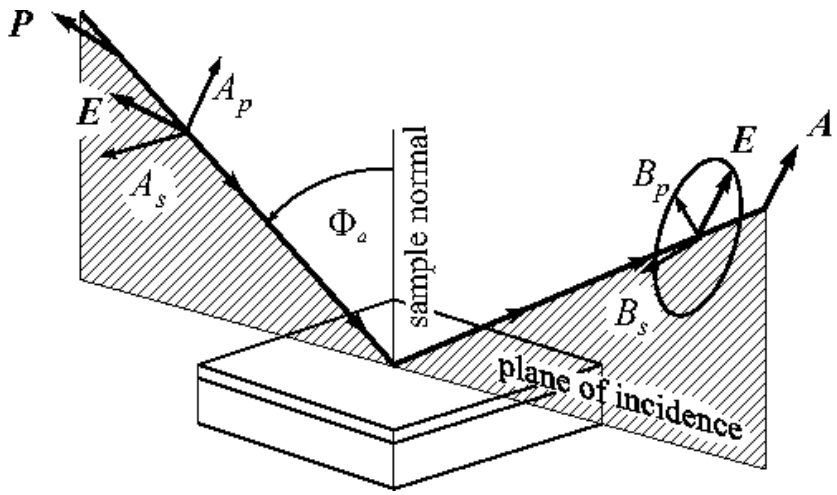

Figure 2.1: Definition of the plane of incidence (p plane) and the incidence angle Φ_{a} through the wave vectors of the incident and emerging (reflection setup) plane waves. A_{p}, A_{s}, B_{p}, and B_{s} denote the complex amplitudes of the p and s modes before and after reflection, respectively. P and A are the azimuth angles of the linear polarizer as used in the standard arrangement of a rotating-analyzer ellipsometer.

ϱ is often presented via real-valued parameters Ψ and Δ, where $\tan(\Psi)$ is the absolute value of the real part of ϱ, and Δ denotes the relative phase change of the p and s components of the electromagnetic wave.

The polarization state change can be described within different frameworks, among them the Jones and Stokes vector systems. For non-depolarizing measurements, the Jones vector system is sufficient. When depolarization is present, e.g., due to the sample or the experimental setup, the Stokes framework, which includes Mueller matrices, should be applied. A Jones vector describes the polarization state of an electromagnetic wave before or after sample interaction, and its entries are the amplitudes of the p and s components. A Jones matrix describes the effect of a linear optical element upon interaction with a plane parallel electromagnetic wave by multiplication with an input Jones vector to yield the corresponding output Jones vector.[14]

$$\begin{pmatrix} B_\mathrm{p} \\ B_\mathrm{s} \end{pmatrix} = \begin{pmatrix} j_\mathrm{pp} & j_\mathrm{sp} \\ j_\mathrm{ps} & j_\mathrm{ss} \end{pmatrix} \begin{pmatrix} A_\mathrm{p} \\ A_\mathrm{s} \end{pmatrix}, \tag{2.2}$$

Off-diagonal entries of a Jones matrix are nonzero for optical elements that convert a portion of the p component to the s component of the electromagnetic wave and *vice versa*. Such situations are encountered, for example, when studying samples with nanostructured surfaces.[17]

For isotropic samples, Ψ and Δ do not depend on the input polarization state, and via the Jones framework, ϱ can be written as

$$\varrho = \frac{j_\mathrm{p}}{j_\mathrm{s}} = \tan(\Psi)\exp(\mathrm{i}\Delta), \tag{2.3}$$

where j_p and j_s denote the p- and s-polarized complex reflection ("$j_\mathrm{p,s}$" = "$r_\mathrm{p,s}$") or transmission ("$j_\mathrm{p,s}$" = "$t_\mathrm{p,s}$") coefficients, respectively.

Because the equations relating Ψ and Δ to physical sample parameters, such as layer thicknesses and optical constants, are nonlinear, a model must be made to describe the optical system. The model incorporates sample geometry, layer structure, and polarizability properties of component materials. Data analysis makes use of nonlinear regression methods, where measured and model-calculated ellipsometry spectra are matched as closely as possible by varying appropriate

model parameters. The details of ellipsometry data analysis are beyond the scope of this work, and interested readers are directed to more thorough discussions in the literature.[18–20]

2.1.1 Pseudodielectric model function approach

The pseudodielectric function $\langle\varepsilon\rangle$ is a common representation of the ellipsometric data Ψ and Δ via the two-phase (ambient-substrate) model.[14,20] The pseudodielectric function eliminates the angle-of-incidence dependence from Ψ and Δ for the ideal optical ambient-substrate model situation.[21–23]

$$\langle\varepsilon\rangle = \varepsilon_\mathrm{a}\left(\left(\frac{1-\varrho}{1+\varrho}\right)^2 \sin^2\Psi_\mathrm{a} + \cos^2\Psi_\mathrm{a}\right)\tan^2\Psi_\mathrm{a}. \tag{2.4}$$

The ambient dielectric function ε_a is unity for normal ambient or vacuum. The pseudodielectric function $\langle\varepsilon\rangle$ is often used to represent the dielectric function of a bulk sample whose surface is not ideally clean, and covered, for example, with organic contaminants, and for electronic surface states that alter the dielectric function in the close vicinity of the surface.

For liquids, the ambient dielectric function ε_a is either measured independently using the minimum deviation technique[24] or taken from standard libraries. Typically, the ambient fluid is transparent in the visible range, so the ambient dielectric function can be represented by the ambient index of refraction n_a.

2.1.2 4×4 transfer matrix modeling approach

The electromagnetic response of layered materials, for example, as presented in Eq. 2.3 can be described through a 4×4 matrix modeling approach, compatible with the Jones or Stokes vector systems, also known as the Berreman-formalism.[14,20,25–28] Fig. 2.2 shows a hypothetical layer stack with input (A and D) and output (B and C) electromagnetic waves; it follows that a reflection setup would force D to zero. A transfer matrix $\mathbf{T}$ describes the optical behavior of the entire structure such that

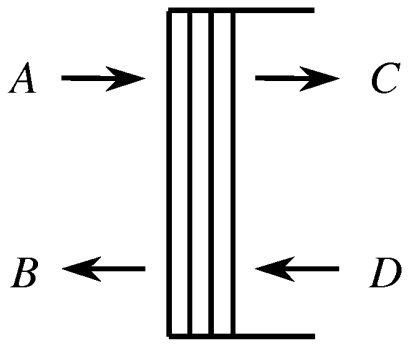

Figure 2.2: Schematic presentation of incident (A), reflected (B), and transmitted (C) plane waves across a sample with plane parallel interfaces, and multiple layer stacks at the front side of the supporting substrate. (Indices for eigenpolarizations, e.g., p and s, and angle of incidence are suppressed.) D modes (if present) are incident from the right. The substrate may totally absorb C and/or D.

$$\begin{pmatrix} A_{\mathrm{s}} \\ B_{\mathrm{s}} \\ A_{\mathrm{p}} \\ B_{\mathrm{p}} \end{pmatrix}_{\text{frontside}} = \begin{pmatrix} T_{11} & T_{12} & T_{13} & T_{14} \\ T_{21} & T_{22} & T_{23} & T_{24} \\ T_{31} & T_{32} & T_{33} & T_{34} \\ T_{41} & T_{42} & T_{43} & T_{44} \end{pmatrix}_{\text{backside}} \begin{pmatrix} C_{\mathrm{s}} \\ D_{\mathrm{s}} \\ C_{\mathrm{p}} \\ D_{\mathrm{p}} \end{pmatrix}_{\text{backside}} . \tag{2.5}$$

A simple algebraic relation exists between matrix elements of $\mathbf{T}$ and ϱ in Eq. 2.3 as defined by

$$\varrho = tan(\Psi)\mathrm{e}^{\mathrm{i}\Delta} = \frac{T_{11}T_{43} - T_{41}T_{13}}{T_{21}T_{33} - T_{23}T_{31}}. \tag{2.6}$$

$\mathbf{T}$ is an ordered product of partial transfer matrices ($\mathbf{T}_{\mathrm{p}}$) and matrices that describe incident (ambient, $\mathbf{L}_{\mathrm{a}}$) and exit (substrate, $\mathbf{L}_{\mathrm{f}}$) mediums. Each $\mathbf{T}_{\mathrm{p}}$ relates the optical properties of a homogenous component layer of the stack. Note that in general none of the matrices $\mathbf{L}_{\mathrm{a}}$, $\mathbf{L}_{\mathrm{f}}$, or $\mathbf{T}_{\mathrm{p}}$ multiplicatively commute. The partial transfer matrices are bracketed, in order of each layer's appearance within the layer stack, by the incident and exit medium matrices, respectively, such that

$$\mathbf{T} = \mathbf{L}_{\mathrm{a}}^{-1}\mathbf{T}_{\mathrm{p,1}}^{-1}\ldots\mathbf{T}_{\mathrm{p,N}}^{-1}\mathbf{L}_{\mathrm{f}}. \tag{2.7}$$

The ambient matrix

$$\mathbf{L}_{\mathrm{a}}^{-1} = \frac{1}{2}\begin{pmatrix} 0 & 1 & -(n_{\mathrm{a}}\cos\Phi_{\mathrm{a}})^{-1} & 0 \\ 0 & 1 & (n_{\mathrm{a}}\cos\Phi_{\mathrm{a}})^{-1} & 0 \\ (\cos\Phi_{\mathrm{a}})^{-1} & 0 & 0 & 1/n_{\mathrm{a}} \\ -(\cos\Phi_{\mathrm{a}})^{-1} & 0 & 0 & 1/n_{\mathrm{a}} \end{pmatrix}, \tag{2.8}$$

is a function of the angle of incidence Φ_{a} and index of refraction n_{a} of the (isotropic) material. The substrate matrix

$$\mathbf{L}_{\mathrm{f}} = \begin{pmatrix} 0 & 0 & \cos\Phi_{\mathrm{f}} & -\cos\Phi_{\mathrm{f}} \\ 1 & 1 & 0 & 0 \\ -N_{\mathrm{f}}\cos\Phi_{\mathrm{f}} & N_{\mathrm{f}}\cos\Phi_{\mathrm{o}} & 0 & 0 \\ 0 & 0 & N_{\mathrm{f}} & N_{\mathrm{f}} \end{pmatrix}, \tag{2.9}$$

depends on the angle of propagation within the exit medium Φ_{f} and the material complex-valued index of refraction $N_{\mathrm{f}} = n_{\mathrm{f}} + \mathrm{i}k_{\mathrm{f}}$. The angle Φ_{f} is calculated from Snell's law,

$$\cos\Phi_{\mathrm{f}} = \sqrt{1 - \left[(n_{\mathrm{a}}/N_{\mathrm{f}})\sin\Phi_{\mathrm{a}}\right]^2}. \tag{2.10}$$

$\mathbf{T}_{\mathrm{p}}$ of a given layer with thickness d and index of refraction n can be obtained from the exponential function,

$$\mathbf{T}_{\mathrm{p}} = \exp\left(\mathrm{i}\frac{\omega}{c}\tilde{\Delta}d\right), \tag{2.11}$$

where c is the speed of light, ω is the light wave orbital frequency, and $\tilde{\Delta}$ is the characteristic matrix of the layer. For isotropic layers,

$$\tilde{\Delta} = \begin{pmatrix} 0 & 0 & 0 & 1 - k_{\mathrm{x}}^2/\varepsilon \\ 0 & 0 & 1 & 0 \\ 0 & k_{\mathrm{x}}^2 - \varepsilon & 0 & 0 \\ \varepsilon & 0 & 0 & 0 \end{pmatrix}. \tag{2.12}$$

For layer j, $\tilde{\Delta}_j$ is a function of its dielectric constant, $\varepsilon_j = (n_j + \mathrm{i}k_j)^2$, and the x-component of the incident wavevector, $k_{\mathrm{x}} = n_{\mathrm{a}}\sin\Phi_{\mathrm{a}}$.

2.1.3 Virtual separation approach

For ultra-thin transparent layers that are small relative to the wavelength of the probing light, $\lambda = 2\pi c/\omega$, such that $2\pi nd/\lambda \ll 1$, which is defined here as the optical ultra-thin film limit, the exponential in Eq. 2.11 can be expanded to a first-order series in d. Thus, for a stack of N very thin sublayers of individual thickness d_j whose total thickness satisfies the condition $d = \sum d_j \ll \lambda/(2\pi n)$, the ordered product in Eq. 2.7 can be approximated by a direct sum, and the order of sublayers with thickness parameters d_j does not affect the result and may be chosen arbitrarily. This can be seen by equivalent results for $\mathbf{T}$ yielded from (a) expanding all exponentials, keeping only terms independent or linear in d_j,

$$\mathbf{T} \approx \mathbf{L}_\mathrm{a}^{-1} \left(1 - \mathrm{i}\frac{\omega}{c}\tilde{\Delta}_1 d_1\right) \times \ldots \times \left(1 - \mathrm{i}\frac{\omega}{c}\tilde{\Delta}_\mathrm{N} d_\mathrm{N}\right) \mathbf{L}_\mathrm{f}, \tag{2.13}$$

$$\mathbf{T} \approx \mathbf{L}_\mathrm{a}^{-1} \left(1 - \mathrm{i}\frac{\omega}{c}\tilde{\Delta}_1 d_1 \ldots - \mathrm{i}\frac{\omega}{c}\tilde{\Delta}_\mathrm{N} d_\mathrm{N}\right) \mathbf{L}_\mathrm{f}, \tag{2.14}$$

and rearranging the order of terms (matrix sum) in the brackets of Eq. 2.14 and (b) rewriting them again in terms of exponentials (matrix products) in Eq. 2.13. Therefore, terms due to individual sublayers may be interchanged, and for any sublayer pair, one obtains

$$\mathbf{T}_{\mathrm{p},1}\mathbf{T}_{\mathrm{p},2} \approx \mathbf{T}_{\mathrm{p},2}\mathbf{T}_{\mathrm{p},1}. \tag{2.15}$$

A porous ultra-thin film is now considered. Because of the film's porosity, neither thickness nor index of refraction are unambiguously defined quantities, and they are named here as d_eff and n_eff, respectively. Let us assume that the ultra-thin film (a) is transparent ($k_\mathrm{eff} = 0$), (b) is optically differentiable from the ambient ($n_\mathrm{eff} \neq n_\mathrm{a}$), and (c) satisfies the condition $d_\mathrm{eff} \ll \lambda/(2\pi n_\mathrm{eff})$.

By exploiting sublayer interchangeability, one is therefore able to segregate the heterogeneous layer into perfectly homogenous sublayers of organic adsorbate (n_o and d_o) and ambient (n_a and d_a) from an ellipsometric modeling point of view. The following relations are then key to the discussed virtual separation approach:

$$\mathbf{T}_{\mathrm{p,eff}} \approx \mathbf{T}_{\mathrm{p,o}}\mathbf{T}_{\mathrm{p,a}} \approx \mathbf{T}_{\mathrm{p,a}}\mathbf{T}_{\mathrm{p,o}}. \tag{2.16}$$

The equivalence to the right implies that the layer with n_{a} can be placed mathematically to the top of the layer stack, and the solvent (ambient) content *within* d_{eff} has no influence on the ellipsometric parameters. As a consequence, the actual ambient content within the heterogenous thin film cannot be detected by any linear polarization-dependent optical experiment. The explicit proof for the latter conclusion is omitted here for brevity; however, it is obvious that a surface layer consisting of pure ambient can neither be sensed nor even be logically described, since its surface (ambient-ambient interface) cannot be optically differentiated. The virtual separation approach, implemented by the left equivalence in Eq. 2.16, holds true if the following two equations are satisfied:

$$d_{\mathrm{eff}} = d_{\mathrm{o}} + d_{\mathrm{a}}, \tag{2.17}$$

$$n_{\mathrm{eff}}^2 = f_{\mathrm{o}}^{\mathrm{V}} n_{\mathrm{o}}^2 + (1 - f_{\mathrm{o}}^{\mathrm{V}}) n_{\mathrm{a}}^2, \tag{2.18}$$

where $f_{\mathrm{o}}^{\mathrm{V}}$ is the volumetric adsorbate fraction of the thin film.

Eq. 2.17 is equivalent to volume conservation, Eq. 2.18 follows from electric charge conservation, and both provide the schemes for connecting the "effective" thickness and the effective index of refraction to the constituents within the virtual separation approach. Note that the number of constituents is not limited to two and can be expanded by adding multiple constituents' parameters to the right sides of Eqs. 2.17 and 2.18, accordingly.

The virtual separation approach renders the linear averaging scheme between the dielectric constants of the embedded materials as a valid effective medium consideration for the mixed-material ultra-thin layer and is different from the commonly known Bruggeman or Maxwell-Garnett effective medium approximations. The latter are derived for three-dimensional mixtures of geometrical inclusions with dimensions much smaller than the probing wavelength. The effective medium consideration changes when approaching a mixture in two dimensions, and the discussed approach in this work presents the correct results for the effective medium mixing in that case.

2.1.4 Parameter accessibility

Formation of an ultra-thin film consisting of a mixture between adsorbate and ambient constituents is experimentally detected by parameters $\delta\Psi$ and $\delta\Delta$, which are the deviations from Ψ and Δ, respectively, that are measured prior to thin film formation. In this case, Ψ and Δ describe the bare substrate within a liquid cell filled with the fluid ambient or with a set of different thin films already present before ultra-thin film formation. $\delta\Psi$ and $\delta\Delta$ depend on the product $n_o d_o$. If n_o can be assumed, e.g., from experimental results or the literature, inversion of the ellipsometric parameters then delivers d_o, which is termed d_{SE} in this work. The SE measurement parameter X^{SE} is defined as the index-thickness product,

$$X^{SE} \equiv n_o d_{SE}. \tag{2.19}$$

One can acquire X^{SE} by constructing an optical model for the experimental system (substrate-organic adsorbate-ambient), describing the dielectric function for each optical model component, and varying X^{SE} in the optical model until experimental data and optical model-generated data best match. Without further proof, it can be shown that the variation in $\delta\Psi$ due to $n_o d_{SE}$ is much less pronounced than in $\delta\Delta$.[16] Therefore, $\delta\Delta$ bears much higher sensitivity to thin film formation and is reported commonly, for example, from real-time *in-situ* measurements of organic ultra-thin film attachment.

Another result of the ultra-thin film approximation is that the index-thickness product cannot be resolved; in addition to systematic and random errors of measured $\delta\Delta$, the relative error for d_{SE} is the same as for the assumed n_o.[13,18,19]

2.2 Quartz crystal microbalance

A quartz crystal microbalance measures vibrational frequency changes of a quartz crystal sensor's odd harmonic resonance overtones. The quartz crystal is cut such that it vibrates in a shear mode due to the piezoelectric effect. The quartz crystal can be coated with metal to act as top and bottom electrode contacts. The sensor top contact is used as the experimental substrate.[29]

For rigid films, the correlation between a frequency shift of $\delta\nu_{\mathrm{N_{ov}}}$, where overtone $\mathrm{N_{ov}} = 3, 5, ...$, and the change in attached mass per unit area Γ_{QCM} is linear and described by the Sauerbrey equation,[30]

$$X^{\mathrm{QCM}} \equiv \rho_{\mathrm{eff}} d_{\mathrm{QCM}} = \Gamma_{\mathrm{QCM}} = -\frac{\delta\nu_{\mathrm{N_{ov}}}\sqrt{\rho_{\mathrm{q}}\mu_{\mathrm{q}}}}{2\nu_0^2 \mathrm{N_{ov}}}, \tag{2.20}$$

where ρ_{eff} is the average, effective density of the ultra-thin film, d_{QCM} is the total thickness of the porous ultra-thin film that includes ambient inclusions, ρ_{q} is the density of quartz, and μ_{q} is the shear modulus of quartz. The QCM measurement parameter is defined here as X^{QCM}, which is commonly reported as the surface density Γ_{QCM}. As explained in Section 2.1.4 for the index-thickness product, the density-thickness product $\rho_{\mathrm{eff}} d_{\mathrm{QCM}}$ also cannot be resolved.

Because the Sauerbrey equation assumes a rigid film scenario, to determine film viscoelasticity, a variation of QCM known as quartz crystal microbalance with dissipation (QCM-D) is used to also measure the shifts in signal dissipation of the odd harmonic overtones.[31] In a manner similar to ellipsometry data analysis, physical film parameters in a viscoelastic model that includes the Voigt constitutive equation, for example, are varied as model-generated frequency and dissipation data are best-matched to experimental results.[31] For the specific application here to ultra-thin films, however, dissipation shifts are typically small, and detected viscoelastic effects do not provide sufficient sensitivity for breaking the density-thickness product. The author therefore limits discussion to the rigid scenario.

2.3 Experimental parameters

Once the measurement parameters X^{SE} and X^{QCM} have been determined, they can be used with assumed or known material properties (volumetric densities and optical indices of refraction) to obtain the thickness (d_{SE} and d_{QCM}) and adsorbate fraction ($f_{\mathrm{o}}^{\mathrm{m}}$ and $f_{\mathrm{o}}^{\mathrm{V}}$ for mass and volume bases, respectively) parameters.

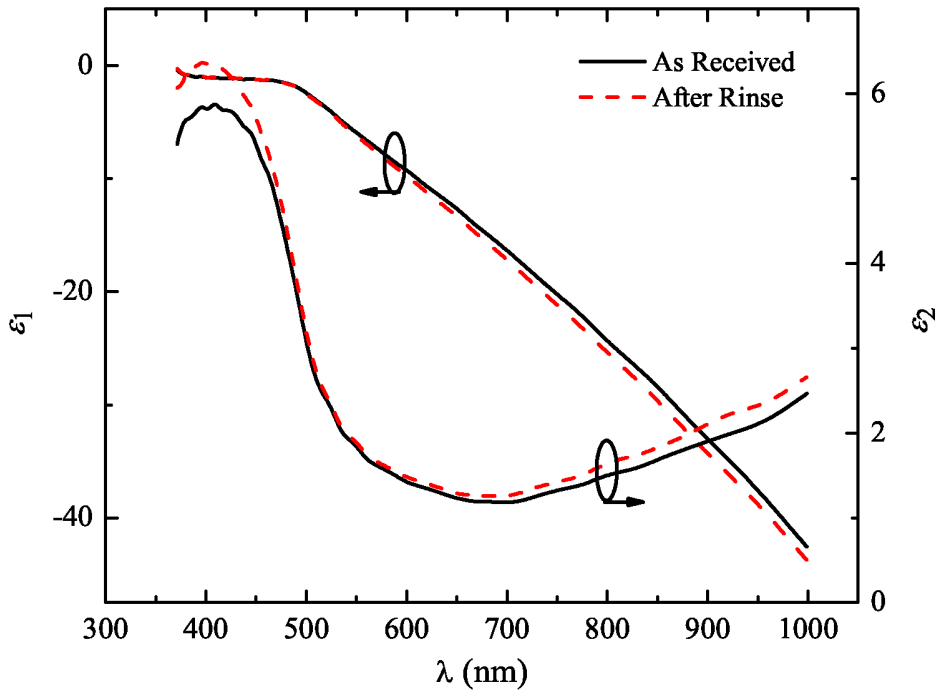

Figure 2.3: Real and imaginary parts of the dielectric function $\varepsilon = \varepsilon_1 + \mathrm{i}\varepsilon_2 = (n + \mathrm{i}k)^2$ measured *in-situ* for the Au QCM-D wafer surface prior to and after the introduction of nanopure water. The "pristine" gold surface was slightly altered by washing away contaminants residing on the surface, reflected here by the overall increase of the imaginary part of the Au dielectric function after insertion of the nanopure water.

2.3.1 Determination of X^{SE}

A layered substrate-organic adsorbate-ambient optical model is used to calculate the ellipsometric response of the sample when the ultra-thin film is being formed or modified. The dielectric function of each component in the optical model must be known. The ellipsometric measurement parameter $X^{\mathrm{SE}} \equiv n_{\mathrm{o}} d_{\mathrm{SE}}$ is obtained by variation of d_{SE} until measured and calculated SE data match as closely as possible. The first step is to measure and determine the substrate dielectric function from a clean surface.

The author has previously discussed changes in the imaginary part of the substrate dielectric function upon introduction of liquid ambient.[32] Fig. 2.3 depicts the real and imaginary parts of the dielectric function $\varepsilon = \varepsilon_1 + \mathrm{i}\varepsilon_2 = (n + \mathrm{i}k)^2$ for the Au surface before and after the introduction of nanopure water. The "pristine" Au surface was slightly altered by washing away contaminants residing on the surface, reflected here by the overall increase of the imaginary part of the Au dielectric function after insertion of the nanopure water. The latter effect was first described by Drude[16,33] and later implemented for measuring the cleanliness of surfaces in ultra-high vacuum conditions.[21,34] As one cannot be certain the substrate surface is absolutely free of organic contaminants prior to ultra-thin film growth, one obtains the substrate dielectric function by determining its pseudodielectric function. The spectral dependence of the substrate pseudodielectric function is conveniently modeled via parameterization using a basis-spline (B-spline) function.[35] The remaining unknown within this model is the index of refraction of the organic thin film. Because the ultra-thin film is assumed to be transparent, its extinction coefficient is set to zero ($k_{\mathrm{o}} = 0$). It is further assumed, without loss of generality, that the index of refraction is wavelength-independent, i.e., $n_{\mathrm{o}}(\lambda) = n_{\mathrm{o}}$.

2.3.2 Determination of fraction and thickness parameters

The quantities n_{o}, ρ_{o}, n_{a}, and ρ_{a} must be known or assumed. d_{SE} can be immediately found from the definition of X^{SE}, where

$$d_{\mathrm{SE}} = \frac{X^{\mathrm{SE}}}{n_{\mathrm{o}}}. \tag{2.21}$$

For the scenario where $\rho_{\mathrm{o}} = \rho_{\mathrm{a}}$, the effective density ρ_{eff} of the ultra-thin film is constant. This scenario is relevant if (a) the adsorbate density is known to be very similar to the ambient density or (b) the adsorbate density cannot be determined. The second justification would apply, for example, if the adsorbate is a powder outside of solution and molecular packing phenomena prevent density measurement. Mass and volume fractions of the ultra-thin film are equivalent.

With ρ_{eff} known, the QCM thickness d_{QCM} is acquired from the definition of X^{QCM}, where

$$d_{\mathrm{QCM}} = \frac{X^{\mathrm{QCM}}}{\rho_{\mathrm{eff}}}. \tag{2.22}$$

The adsorbate content fraction $f_{\mathrm{o}}^{\mathrm{m,V}} = f_{\mathrm{o}}^{\mathrm{m}} = f_{\mathrm{o}}^{\mathrm{V}}$ is given by

$$f_{\mathrm{o}}^{\mathrm{m,V}} = \frac{d_{\mathrm{SE}}}{d_{\mathrm{QCM}}}. \tag{2.23}$$

In the scenario of different densities for the adsorbate and ambient, ρ_{eff} may vary with time during a dynamic measurement as the porosity changes. Consequently, mass and volume fraction parameters may be different.

$$f_{\mathrm{o}}^{\mathrm{m}} = \frac{m_{\mathrm{o}}}{m_{\mathrm{o}} + m_{\mathrm{a}}} = \frac{m_{\mathrm{o}}}{m_{\mathrm{eff}}}, \tag{2.24}$$

$$f_{\mathrm{o}}^{\mathrm{V}} = \frac{V_{\mathrm{o}}}{V_{\mathrm{o}} + V_{\mathrm{a}}} = \frac{V_{\mathrm{o}}}{V_{\mathrm{eff}}}, \tag{2.25}$$

where m_{o} (V_{o}) is the adsorbate mass (volume), m_{a} (V_{a}) is the mass (volume) of ambient inclusions, and m_{eff} (V_{eff}) is the total ultra-thin film mass (volume).

The masses in Eq. 2.24 can be rewritten as density-thickness-area products to find $f_{\mathrm{o}}^{\mathrm{m}}$, such that

$$f_{\mathrm{o}}^{\mathrm{m}} = \frac{\rho_{\mathrm{o}} d_{\mathrm{SE}} A}{\rho_{\mathrm{eff}} d_{\mathrm{QCM}} A} = \frac{\rho_{\mathrm{o}} d_{\mathrm{SE}}}{\rho_{\mathrm{eff}} d_{\mathrm{QCM}}}. \tag{2.26}$$

An arbitrary area of the sample is described by A, which is simplified out of Eq. 2.26 because the arbitrary area is the same whether the ultra-thin film includes

ambient inclusions or not. Because neither d_{QCM} nor ρ_{eff} is known at the moment, Eq. 2.26 is rewritten in terms of the SE and QCM measurement parameters to take the following form:

$$f_{\mathrm{o}}^{\mathrm{m}} = \frac{\rho_{\mathrm{o}}}{n_{\mathrm{o}}} \frac{X^{\mathrm{SE}}}{X^{\mathrm{QCM}}}. \tag{2.27}$$

Thus, $f_{\mathrm{o}}^{\mathrm{m}}$ is obtained from a measurement if ρ_{o} and n_{o} are known or can be assumed.

We identify ρ_{eff} as the weighted average of the component densities, such that

$$\rho_{\mathrm{eff}} = f_{\mathrm{o}}^{\mathrm{V}} \rho_{\mathrm{o}} + \left(1 - f_{\mathrm{o}}^{\mathrm{V}}\right) \rho_{\mathrm{a}}. \tag{2.28}$$

It can be shown that

$$f_{\mathrm{o}}^{\mathrm{V}} = \frac{\rho_{\mathrm{eff}}}{\rho_{\mathrm{o}}} f_{\mathrm{o}}^{\mathrm{m}}. \tag{2.29}$$

By combining Eq. 2.28 and Eq. 2.29, one obtains $f_{\mathrm{o}}^{\mathrm{V}}$.

$$f_{\mathrm{o}}^{\mathrm{V}} = \frac{\rho_{\mathrm{a}}}{\rho_{\mathrm{o}}} \frac{f_{\mathrm{o}}^{\mathrm{m}}}{1 - f_{\mathrm{o}}^{\mathrm{m}} + f_{\mathrm{o}}^{\mathrm{m}} \frac{\rho_{\mathrm{a}}}{\rho_{\mathrm{o}}}}, \tag{2.30}$$

which allows ρ_{eff} to be found from Eq. 2.28. Finally, d_{QCM} is found from Eq. 2.22.

2.3.3 Comparison of thickness and surface density parameters

Whether to report the quantity of ultra-thin film attachment as a thickness (d) or surface density (Γ) parameter is a matter of preference. The algorithm to obtain the fraction parameters does not change significantly if surface density parameters are maintained. Note that when ρ_{o} or ρ_{eff} equals $1\,\frac{\mathrm{g}}{\mathrm{mL}}$, the respective thickness parameter in units of nm is equal in magnitude to the respective surface density parameter, $\Gamma_{\mathrm{QCM}} = \rho_{\mathrm{eff}} d_{\mathrm{QCM}}$ and $\Gamma_{\mathrm{SE}} = \rho_{\mathrm{o}} d_{\mathrm{SE}}$, in units of $\frac{\mathrm{mg}}{\mathrm{m}^2}$.

Chapter 3

Combinatorial approach to characterize ultra-thin films

3.1 Experimental setup

Fig. 3.1 illustrates the temperature-controlled liquid cell where ultra-thin films are measured. The liquid cell acts as a lid, and the QCM sensor provides the bottom seal with an O-ring. Fluid inlet and outlet ports allow for ambient liquid solution exchange, and windowed optical channels at a 65° angle of incidence from the QCM sensor normal allow the ellipsometry beam to proceed through the cell and measure the sample.

Fig. 3.2 shows a schematic for the entire experimental setup, including the multiple-inlet fluid control system. The nomenclature for italicized symbols that represent control parameters is given in Table 3.1. Inlet reservoirs R_s contain fluids that can be pumped by respective inlet pumps P_s through a multiple-port valve V_c and a bypass valve V_b. V_b allows the user to redirect flow to R_d and avoid the liquid cell. The fluid then proceeds through the temperature-controlled liquid cell and an optional/alternative drain pump P_d before removal to a drain reservoir R_d. The pumps, valves, and liquid cell temperature are computer-controlled via user interfaces.

The SE and QCM are controlled via computer interface and acquire measurements simultaneously. Each data set that partially constitutes a dynamic mea-

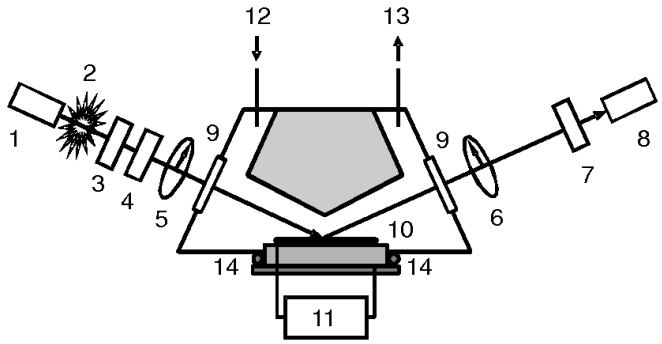

Figure 3.1: Schematic of the experimental liquid cell. 1-tungsten light source, 2-unpolarized light, 3-polarizer, 4-rotating compensator, 5-polarized light, 6-polarized light altered by sample surface, 7-analyzer, 8- detector, 9-optical windows, 10-QCM sensor surface, 11-QCM sensor control, 12-liquid inlet, 13-liquid outlet, 14-O-ring for sealing.

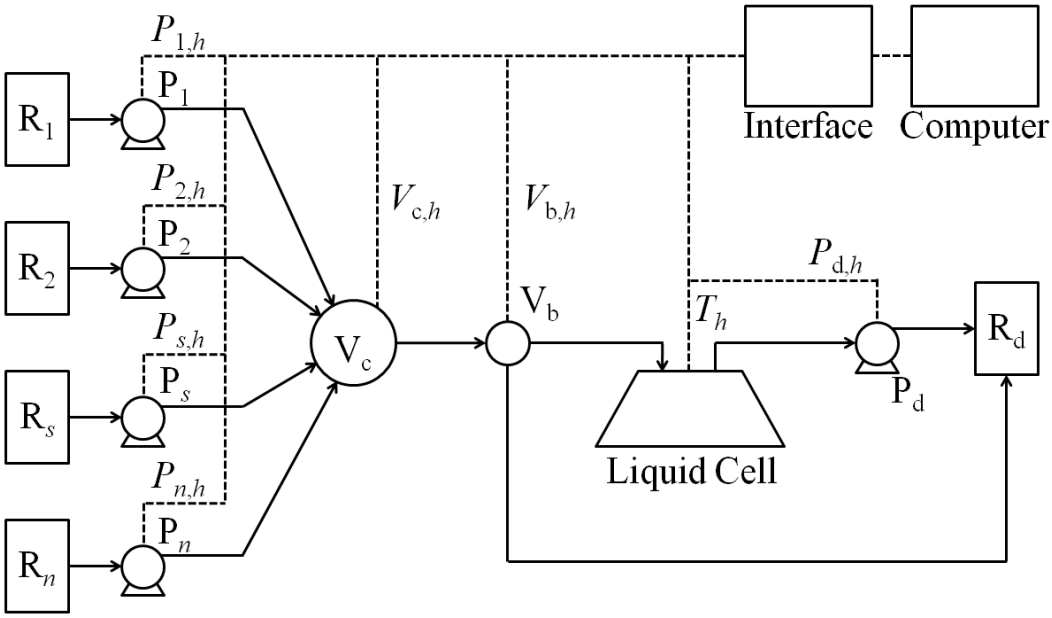

Figure 3.2: Schematic of the experimental setup. Solid lines represent fluid lines, and dotted lines represent an electronic logic control connection.

Parameter	$t = 0$	$t = \tau$	...	$t = h\tau$
$P_{s,h}$	$P_{s,0}$	$P_{s,1}$	...	$P_{s,h}$
$P_{\mathrm{d},h}$	$P_{\mathrm{d},0}$	$P_{\mathrm{d},1}$	...	$P_{\mathrm{d},h}$
$V_{\mathrm{c},h}$	$V_{\mathrm{c},0}$	$V_{\mathrm{c},1}$	...	$V_{\mathrm{c},h}$
$V_{\mathrm{b},h}$	$V_{\mathrm{b},0}$	$V_{\mathrm{b},1}$	...	$V_{\mathrm{b},h}$
T_h	T_0	T_1	...	T_h

Table 3.1: Notation for controlled experimental parameters. The inlet pumps, drain pump, multiple-port valve, bypass valve, and liquid cell temperature are controlled by parameter sets $P_{s,h}$, $P_{\mathrm{d},h}$, $V_{\mathrm{c},h}$, $V_{\mathrm{b},h}$, and T_h, respectively. Upon each measurement period τ, the next set of equipment parameters is called. $h = 0, 1, \ldots, m-1$ where m is an integer that defines the total number of data sets in a dynamic measurement.

surement is taken at a particular time slice. The measurement period τ is defined as the amount of time between two consecutive data sets, and the total number of data sets in a dynamic measurement is m. τ and m are adjusted and set by the user prior to the beginning of a dynamic measurement. The time slice of a data set or control parameter is identified by the integer subscript $h = 0, 1, ..., m-1$.

The inlet pumps, drain pump, multiple-port valve, bypass valve, and liquid cell temperature have control parameter sets $P_{s,h}$, $P_{\mathrm{d},h}$, $V_{\mathrm{c},h}$, $V_{\mathrm{b},h}$, and T_h, respectively. At every time slice of a dynamic measurement, each parameter set has its values predefined in the user interface. For example, at time $t = h\tau$, $P_{s,h}$ may be the flow rate for the inlet pump P_s, and $V_{\mathrm{c},h}$ could be an ordered set of s on or off designations, represented by 1 or 0, respectively, to denote what inlet lines are opened or closed by the multiple-port valve $\mathrm{V_c}$.

3.2 Data acquisition procedures

Fig. 3.3 illustrates the SE/QCM data acquisition procedure. The total length of a dynamic measurement is implied by Fig. 3.3 as the product $m\tau$. Before the dynamic measurement, three separate SE-only data sets are taken. First, the

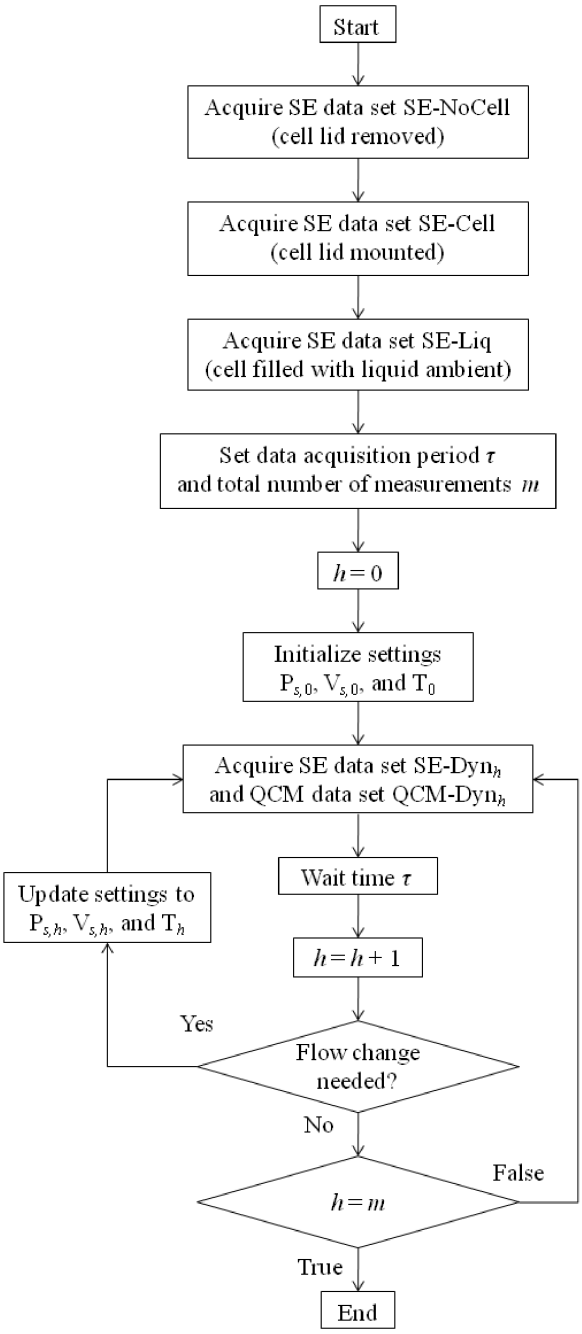

Figure 3.3: Data acquisition flowchart.

liquid cell lid is removed, and a new quartz sensor is placed on the liquid cell bottom. The SE angle of incidence is set to the liquid cell's machined optical port angle (65°), and an SE measurement, denoted here as "SE-NoCell," is taken. Next, the liquid cell lid is attached with the quartz sensor inside. The SE angle of incidence is then adjusted so the probing light beam can proceed through the liquid cell, if necessary. SE measurement "SE-Cell" is acquired at this point. Next, the liquid cell is filled with the liquid ambient of choice, and SE measurement "SE-Liq" is then taken.

At this point, the dynamic measurement is ready to begin, and τ and m are set. To start the dynamic measurement, SE and QCM data sets "SE-Dyn$_0$" and "QCM-Dyn$_0$," respectively, are taken while initial ($h = 0$) flow parameters are in effect. At the hth period of τ time in the dynamic measurement, the current SE and QCM data sets are SE-Dyn$_h$ and QCM-Dyn$_h$, respectively. If the preset flow parameters change at the hth period, the controlled flow units are updated. The final data set is recorded at time slice $m - 1$, and the dynamic measurement ends one period of τ time later.

3.3 Data analysis procedures

The raw SE and QCM data are analyzed through the protocol summarized by Fig. 3.4. The optical model described in Section II can now be built by incorporating the three separate SE data sets. Substrate B-spline function parameters, offsets due to window and angle-of-incidence effects, and substrate modification due to liquid rinsing are accounted for by best-matching SE-NoCell, SE-Cell, and SE-Liq data, respectively, to data generated by the optical model. The index-thickness product X^{SE} that describes the adsorbate component of the organic ultra-thin film is then added to the optical model. X^{SE} is varied with best-matching for every time slice in the dynamic SE data set SE-Dyn$_h$.

d_{SE} is found for each time slice of SE-Dyn$_h$ by Eq. 2.21, assuming n_{o}. Next, Eq. 2.20 is used to find X^{QCM} from QCM-Dyn$_h$.

If identical ρ_{o} and ρ_{a} are assumed (Scenario 1 from Section 2.3.2), one has $\rho_{\mathrm{eff}} = \rho_{\mathrm{o}} = \rho_{\mathrm{a}}$, and Eq. 2.22 is used to find d_{QCM}. The adsorbate fraction parameter for

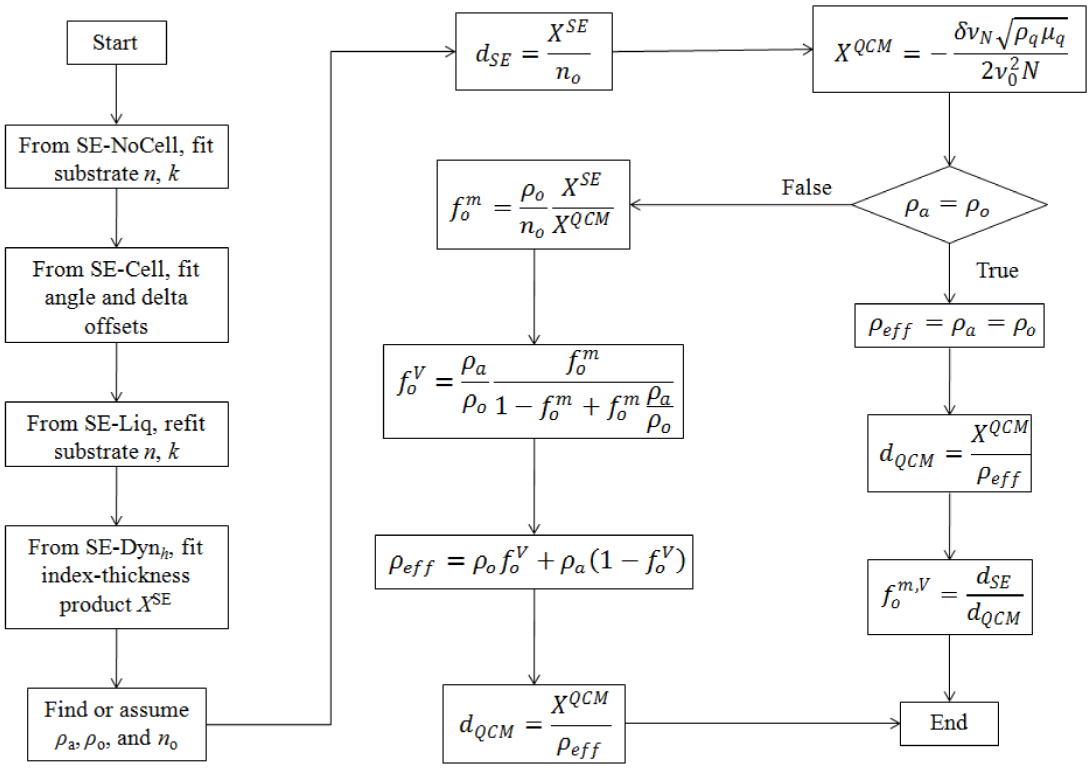

Figure 3.4: Data analysis flowchart.

both mass and volume can then be found for each time slice of data via Eq. 2.23.

If ρ_o and ρ_a are different (Scenario 2 from Section 2.3.2), Eq. 2.27 is used to find f_o^m. f_o^V can then be found from Eq. 2.30. Then ρ_{eff} for each time slice is found from Eq. 2.28. Finally, d_{QCM} is calculated from Eq. 2.22.

3.4 Experimental apparatuses

A commercially available liquid cell equipped with a QCM-D apparatus (Q-Sense E1 SE/QCM-D Module, Biolin Scientific) and optical access windows was set up with a spectroscopic ellipsometer (M-2000-UV, J.A. Woollam Co.). The liquid cell was designed to promote optimal flow effects, avoid disruption via air bubbles, and use a low volume to conserve fluid (Fig. 3.1). The ellipsometer measures 512 wavelengths simultaneously in the spectral region from 370 to 1000 nm. The windows in the liquid cell allow for optical access for SE measurements at a 65° angle of incidence. The liquid cell is equipped with temperature control and air-sealed inlet and outlet lines for the introduction and exchange of solutions. The bottom of the liquid cell is connected to the QCM-D instrumentation. The software, CompleteEASE® (J.A. Woollam Co.) and QSoft™(Biolin Scientific), control the M-2000-UV and E1 QCM-D data acquisition, respectively, and QSoft also controls the temperature of the liquid cell. Control of liquid flow, rate, and times can be achieved with a high-performance liquid chromatography (HPLC) system, such as the Agilent 1200 Infinity LC.

Chapter 4

Measurements

4.1 Surfactant adsorption

Cetyltrimethylammonium bromide (CTAB) is a cationic surfactant with a nonpolar hydrocarbon "tail" and an ammonium salt "head" group. At approximately 1 mM, the critical micelle concentration (CMC), full micelles are formed in aqueous CTAB solutions, where the nonpolar tails are shielded by the polar head groups.[36] Surfactants like CTAB are useful for nanoparticle synthesis[37] and detergent applications.[38]

2.5 mM and 0.1 mM CTAB aqueous solutions were made with no additives. The CTAB was purchased from Sigma-Aldrich, and 18.2 MΩ cm water was prepared from a Barnstead Nanopure water purification system. For data analysis, n_o was assumed to be 1.5, and ρ_a is approximately $1\,\frac{g}{mL}$. The value of ρ_o was not readily known, as dry CTAB is a solid at standard conditions, and effects including packing density must be considered. It was decided to simply set ρ_o to $1\,\frac{g}{mL}$. As a result, the first scenario of data analysis in Fig. 3.4 was used to derive the thickness and adsorbate fraction parameters.

The 2.5 mM CTAB experiments were operated in different liquid cells and with different pumps to highlight liquid flow effects on acquired data. Details of the liquid cells and pumps are provided in Section 5.1.1. The single-rinse 2.5 mM CTAB experiment first entailed the flow of water through the liquid cell to achieve a stable baseline. Next CTAB solution was introduced into the liquid cell. After

approximately 10 min, the inlet source was changed to water, and a rinsing process was observed. The pump speed was 0.4 $\frac{\text{mL}}{\text{min}}$.

The double-rinse 2.5 mM CTAB experiment comprised two CTAB solution introduction and water rinse cycles. The pump speed at the beginning of the measurement was 0.1 $\frac{\text{mL}}{\text{min}}$. CTAB solution flowed through the cell for approximately 16 min. After the first water rinse, the pump speed was increased to 0.5 $\frac{\text{mL}}{\text{min}}$. The second introduction of CTAB solution had a duration of approximately 8 min. A final water rinse then proceeded.

For the 0.1 mM CTAB experiment, water was introduced from its respective reservoir through the liquid cell at 0.4 $\frac{\text{mL}}{\text{min}}$ to achieve a stable baseline. Next, a valve was turned to switch the reservoir to that containing the CTAB solution. After approximately 10 min of CTAB solution flow, the valve was reversed, and approximately 10 min of water flow was allowed before the experiment ended.

4.1.1 2.5 mM CTAB

Raw $\delta\Delta$, $\delta\nu_{\text{N}_{\text{ov}}}$, and $\delta D_{\text{N}_{\text{ov}}}$ for the single-rinse 2.5 mM CTAB experiment are shown in Figs. 4.1, 4.2, and 4.3, respectively. The dissipation data is not used in data analysis because the magnitude of the dissipation shift (in units of 10^{-6}) for CTAB adsorption was very small (approximately 5%) relative to the magnitude of the respective frequency shift (in units of Hz).

The thickness and adsorbate fraction parameters for the single-rinse and double-rinse 2.5 mM CTAB measurements are shown in Figs. 4.4 and 4.5, respectively. The differences between the features of the thickness and adsorbate fraction parameters are suggested here to be due to variations in the liquid flow as described in further detail in Section 5.1.1.

4.1.2 0.1 mM CTAB

Thickness and adsorbate fraction plots for a single adsorption-rinse cycle of 0.1 mM CTAB are shown in Fig. 4.6. CTAB entered the liquid cell at approximately $t = 12$ min, and the nanopure water rinse began at $t = 20$ min. The thickness parameters show monotonic growth and decay during CTAB adsorption and water

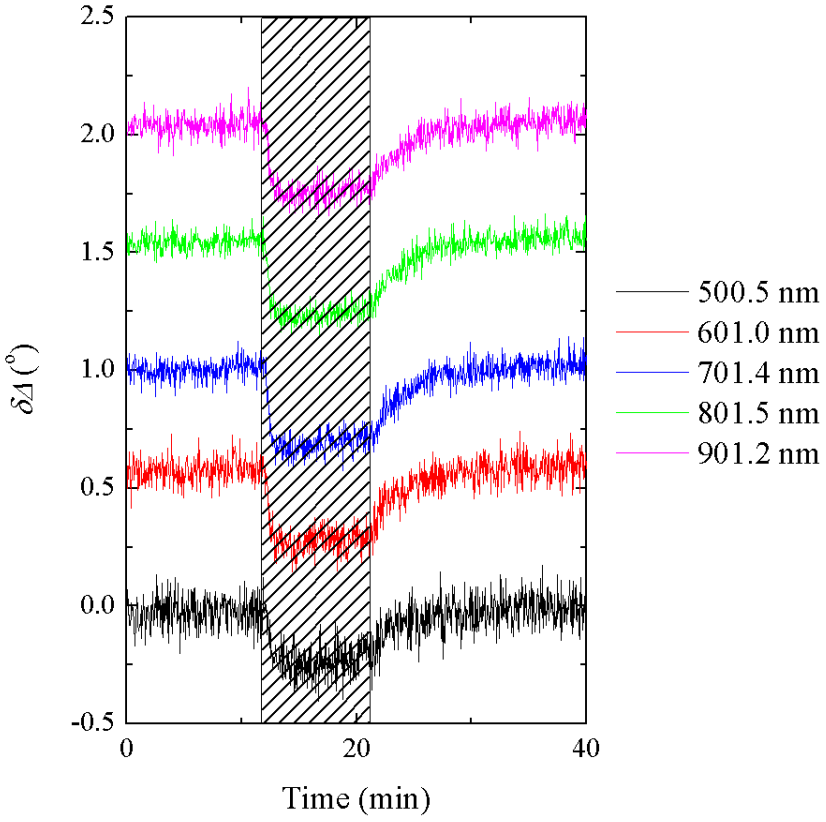

Figure 4.1: Experimental SE data ($\delta\Delta$ only) at selected wavelengths, relative to data measured prior to CTAB incorporation, during introduction of 2.5 mM CTAB for approximately 10 min, followed by a purified water rinse. Data for wavelengths are shifted sequentially by 5° for convenience. The graph is shaded when CTAB is directed into the liquid cell.

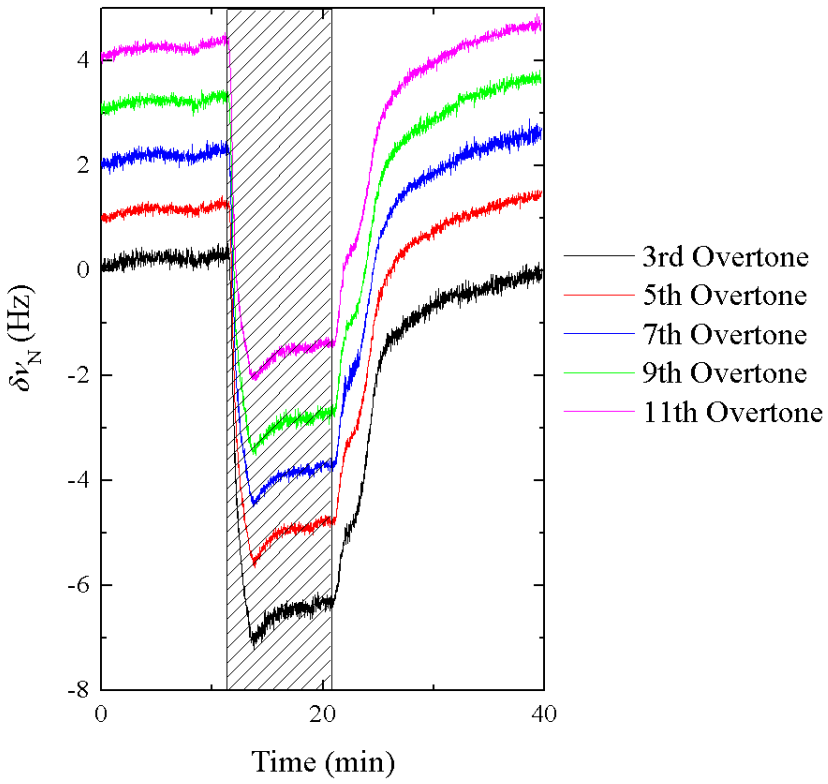

Figure 4.2: QCM-D overtone frequency shifts ($\delta\nu_{N_{ov}}$) during the 2.5 mM CTAB experiment. Data for higher overtones are shifted sequentially by 1 Hz for convenience. The graph is shaded when CTAB is directed into the liquid cell.

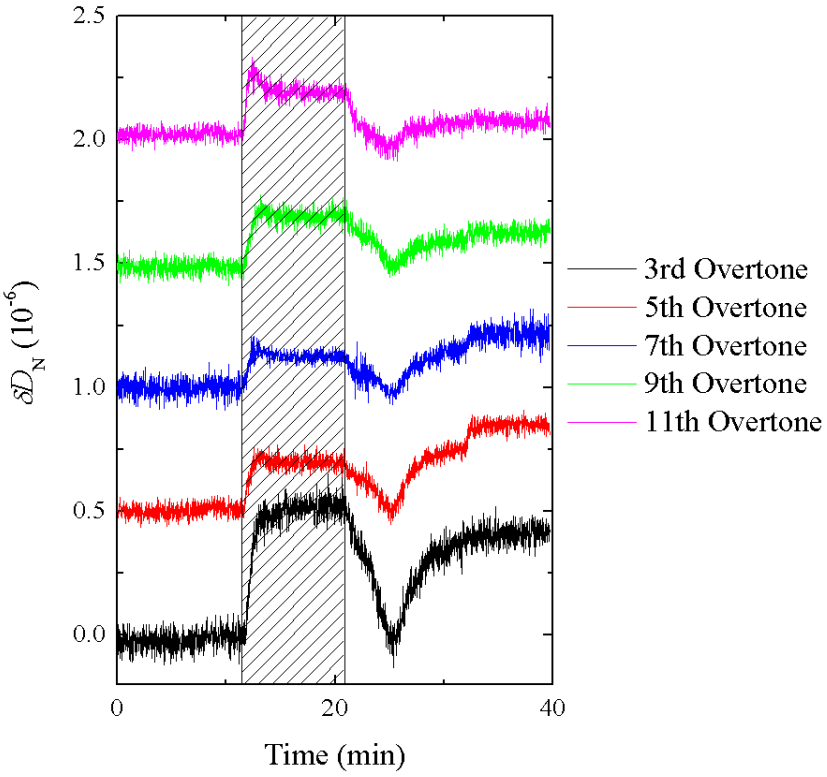

Figure 4.3: QCM-D overtone dissipation shifts ($\delta D_{N_{ov}}$) during the 2.5 mM CTAB experiment. Data for higher overtones are shifted sequentially by $0.5 * 10^{-6}$ for convenience. The graph is shaded when CTAB is directed into the liquid cell.

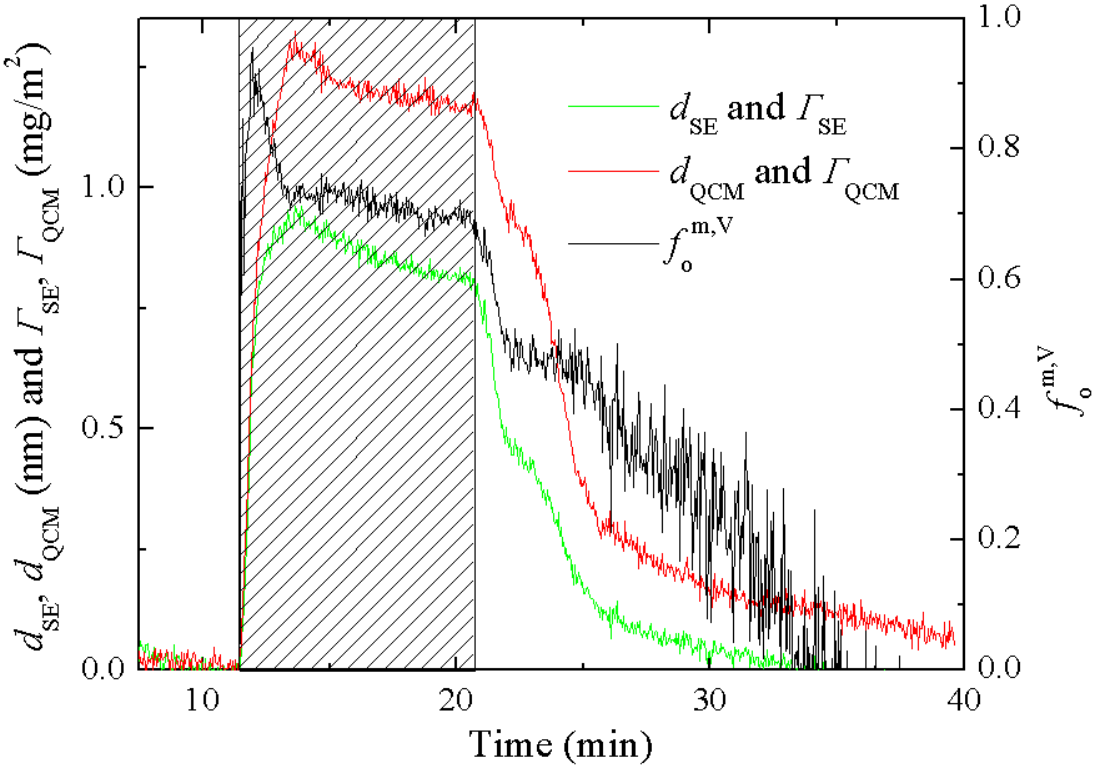

Figure 4.4: Thickness, surface density, and adsorbate fraction parameter plots of single-rinse 2.5 mM CTAB solution experiment reported from SE and QCM measurements. Note that because $\rho_o = \rho_a = \rho_{eff} = 1\,\frac{g}{mL}$, the magnitudes of d in units of nm and Γ in units of $\frac{mg}{m^2}$ are identical. The graph is shaded when CTAB is directed into the liquid cell.

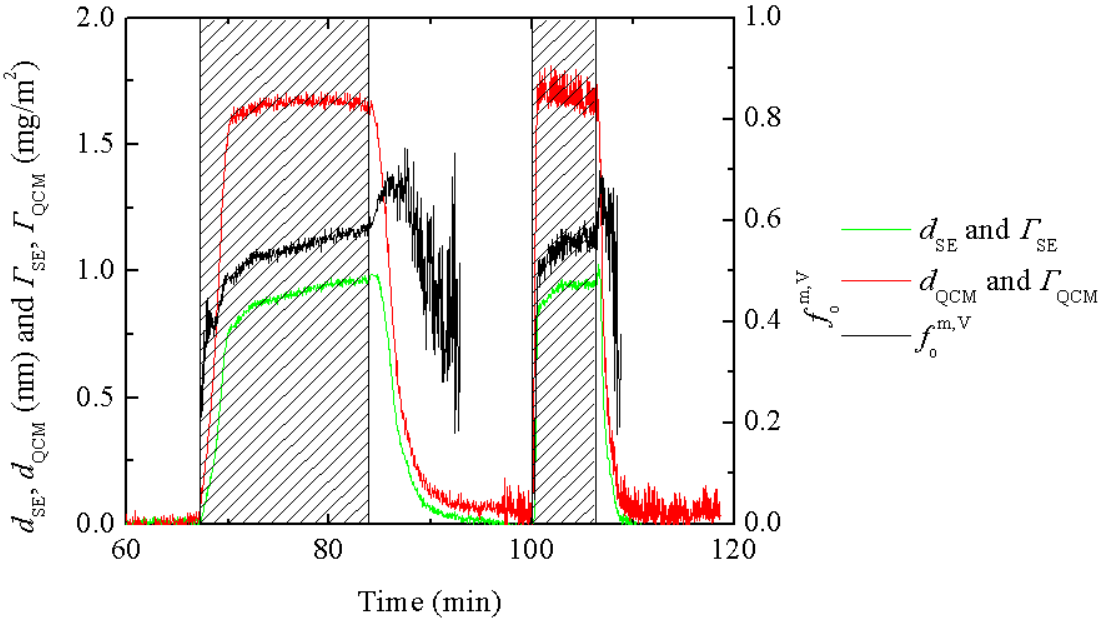

Figure 4.5: Thickness, surface density, and adsorbate fraction parameter plots of double-rinse 2.5 mM CTAB solution experiment reported from SE and QCM measurements. Note that because $\rho_o = \rho_a = \rho_{eff} = 1\,\frac{g}{mL}$, the magnitudes of d in units of nm and Γ in units of $\frac{mg}{m^2}$ are identical. The graph is shaded when CTAB is directed into the liquid cell.

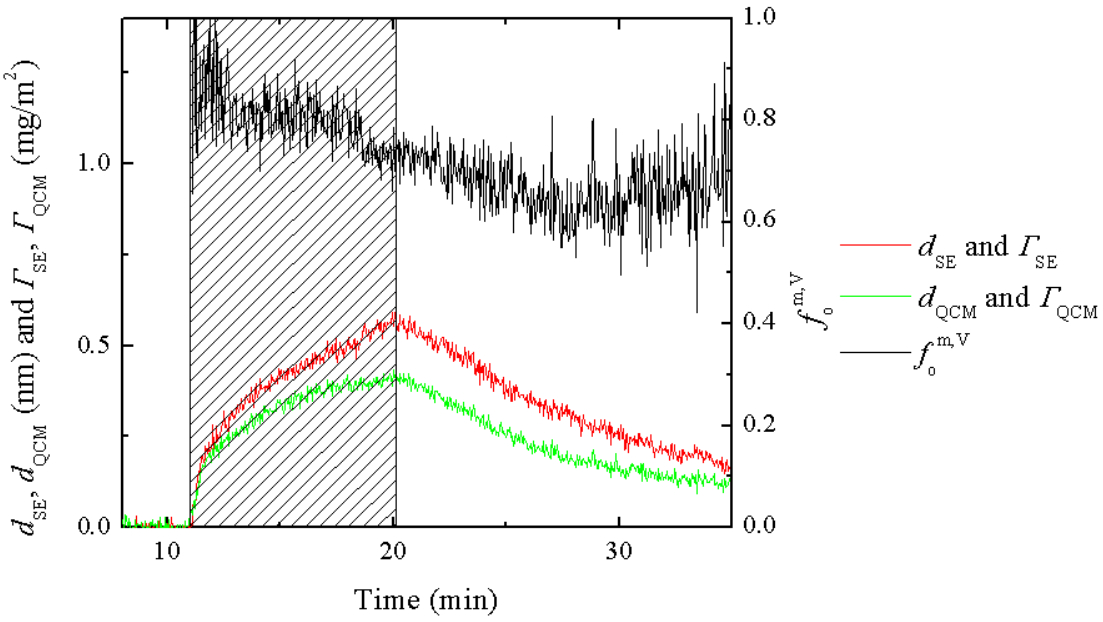

Figure 4.6: Thickness, surface density, and adsorbate fraction parameter plots of 0.1 mM CTAB solution experiment reported from SE and QCM measurements. Note that because $\rho_o = \rho_a = \rho_{eff} = 1\,\frac{g}{mL}$, the magnitudes of d in units of nm and Γ in units of $\frac{mg}{m^2}$ are identical. The graph is shaded when CTAB is directed into the liquid cell.

rinsing, respectively, and the adsorbate fraction parameter remains in the range of 0.7-0.8 through most of the experiment.

4.2 Self-assembled monolayer chemisorption

Alkanethiol self-assembled monolayers (SAMs) are hydrocarbons with a sulfur head group, a hydrocarbon chain body, and a functionalized tail group that exhibits a desired surface chemistry. The sulfur head group binds to the substrate via chemisorption.[39] SAMs are useful as uniform, cost-effective coatings for adjusting a substrate's surface properties.[39] The author has shown 1-decanethiol chemisorption onto Au from an ethanol solution as monitored by SE/QCM.[40] Here a similar scenario, but of 8-mercapto-1-octanol in an aqueous solution, is demonstrated.

8-mercapto-1-octanol was purchased from Sigma-Aldrich and used to prepare a 2 mM solution in purified water with no additives. Pure water and alkanethiol solution had separate reservoirs and pumps that pushed the solutions at 0.1 $\frac{\text{mL}}{\text{min}}$ through V_c, V_b, and the liquid cell to R_d. In similar fashion to the CTAB experiment, once a desired baseline had been reached, the inlet fluid was switched from water to alkanethiol solution. After approximately 100 min, the alkanethiol pump was turned off, and the solution over the quartz sensor became stagnant as the measurement continued overnight.

For this system measured values of $n_\text{o} = 1.484$ and $\rho_\text{o} = 0.93\,\frac{\text{mg}}{\text{mL}}$ (Sigma-Aldrich) were used. Therefore, the $\rho_\text{o} \neq \rho_\text{a}$ scenario was used for analyzing the SAM chemisorption data.

The results for the SAM chemisorption experiment are shown in Fig. 4.7. At $t = 150$ min, two distinct stages in the SAM chemisorption process are evident, in agreement with the literature.[39] f_o^V is uniform throughout the measurement, implying that the porosity is consistent throughout the ultra-thin film growth.

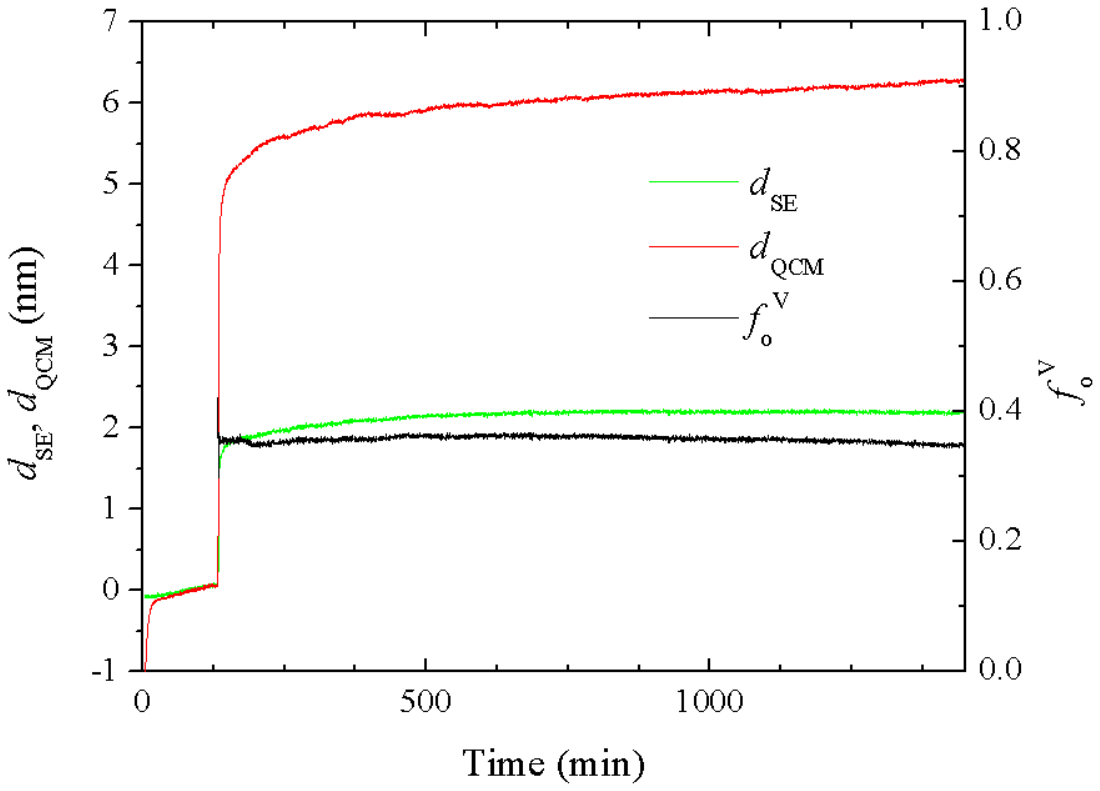

Figure 4.7: Thickness and adsorbate fraction plots of 2 mM 8-mercapto-1-octanol solution experiment reported by SE and QCM. A fast initial growth step is followed by a slower second process, and the porosity represented by the adsorbate fraction parameter is consistent throughout chemisorption.

4.3 Selective DNA detection

SAMs that incorporate single-stranded DNA molecules are widely used for analytical applications that include genotyping,[41] protein and small molecule detection,[42,43] and high-throughput affinity screening.[44] Characterizing the formation and interrogation of DNA-based sensors using SE/QCM has the potential to elucidate factors that contribute to sensor response, such as surface conformation and hybridization efficiency. The probe sequence used here is a well-characterized genosensor specific for a region surrounding codon 12 of the *K-ras* gene, mutations of which are often present in pancreatic cancer lesions.[45]

The DNA probe was conjugated to a six-carbon alkanethiol moiety for attachment to a Au substrate and subsequently embedded with a SAM of 6-mercapto-1-hexanol to enhance stability. It is here demonstrated that SE/QCM is capable of characterizing sub-nanometer average thickness changes and the porosity of multiple-component, biological, ultra-thin films.

To study the utility of SE/QCM in the characterization of bioactive films, DNA sensors were fabricated and interrogated *in-situ*. The running buffer (20 mM Tris, 140 mM NaCl, 5 mM KCl, 1 mM $CaCl_2$, 1 mM $MgCl_2$, pH 7.4, filtered with a 0.2 μm syringe filter immediately before use) was used to make all solutions and was exchanged into the liquid cell as a rinse between each step of sensor fabrication and interrogation. *K-ras* stem-loop DNA probe and BRCA2 and *K-ras* targets were purchased from Biosearch Technologies (Novato, CA). All salts, Tris buffer, and 6-mercapto-1-hexanol were purchased from Sigma-Aldrich. Tris(2-carboxyethyl)phosphine was purchased from Soltec Ventures (Beverly, MA). A flow rate of 50 $\frac{\mu L}{min}$ was used throughout the experiment. Here $n_o = 1.5$ and $\rho_o = 1 \frac{mg}{mL}$ were assumed. General values were chosen to reflect the variety of organic materials that composed the ultra-thin film.

Fig. 4.8 presents changes in thickness and porosity associated with probe chemisorption,[46] 2 mM 1-mercapto-6-hexanol SAM formation, and interrogation with non-complementary[47] and complementary[48] DNA fragments. d_{SE} reflects the dry thickness of the multiple-component layer and does not distinguish between constituent adsorbate materials. d_{QCM} includes d_{SE} and ambient

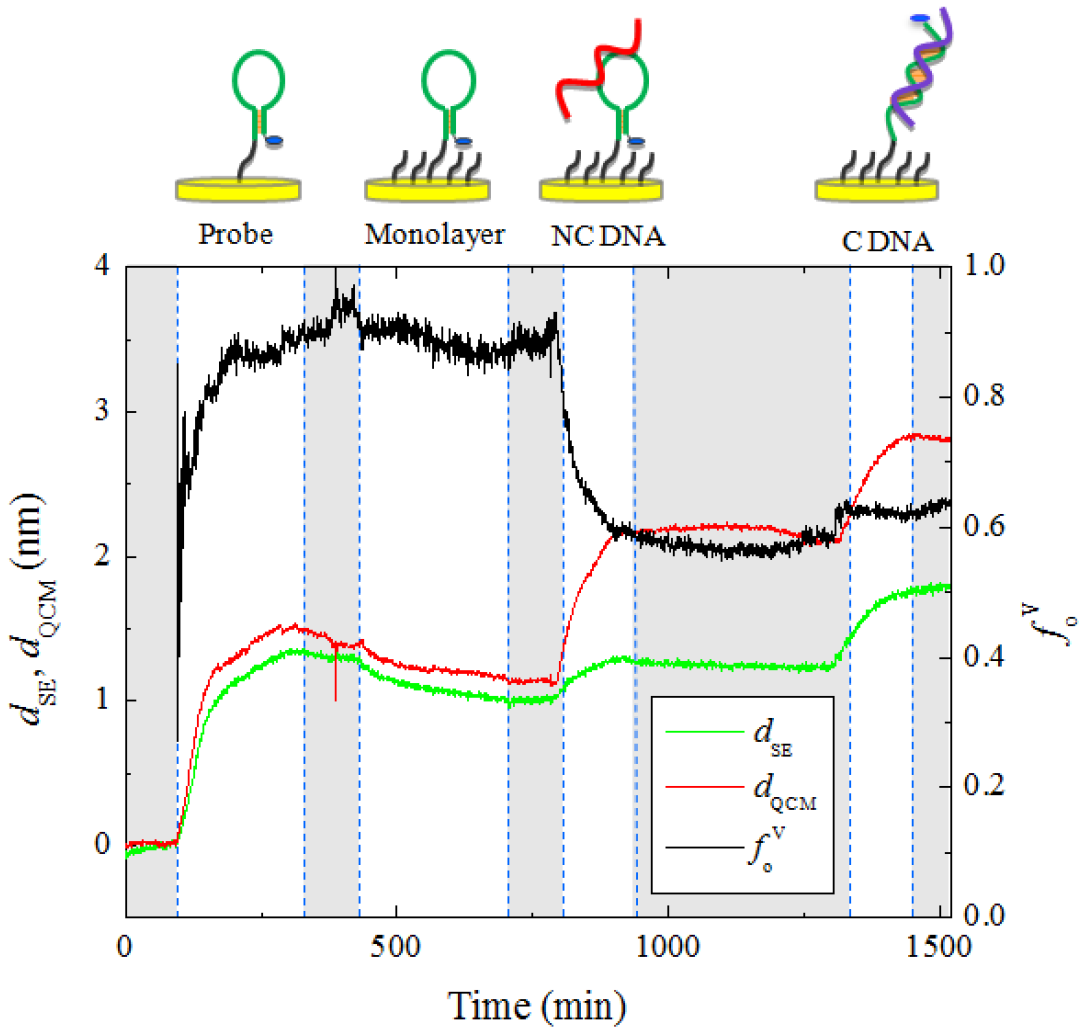

Figure 4.8: Thickness and adsorbate fraction plots of a multiple-component organic film. Insertions of probe aptamer, SAM, non-complementary DNA, and complementary DNA are denoted by Probe, Monolayer, NC DNA, and C DNA, respectively. Note the decrease in thickness upon SAM chemisorption, the shifts in adsorbate fraction when non-complementary and complementary DNA are introduced, and the differences between SE and QCM responses for non-complementary and complementary DNA interrogation. The graph is shaded when buffer solution rinses proceed through the liquid cell.

inclusions. The thickness parameters for the multiple-component layer remain below the optical ultra-thin film limit.

Chapter 5

Discussion

5.1 The roles of liquid flow and QCM-D stability

It is important to identify and account for data artifacts. Two types of data artifacts discussed in more detail are due to liquid flow and QCM-D stability. The 2.5 mM CTAB measurements, in particular, highlight these issues and are therefore the subject of discussion.

5.1.1 Liquid flow

Liquid flow can have significant effects on SE/QCM measurements. The experiments took place in one of two different liquid cells. As shown by Fig. 5.1, both liquid cells had four inlet/outlet holes; one over each window, along the liquid cell x-axis, and two directly over the quartz crystal, vertically along the liquid cell y-axis. The window holes on the x-axis were used as outlet holes for both liquid cells. Liquid Cell A had both vertically aligned holes as inlets, while Liquid Cell B liquid cell had one vertically aligned hole for the inlet and the other for an outlet. Tubing ports connected the liquid cell with the valves, pumps, and reservoirs of the experimental setup. Liquid Cell A had one inlet tubing port and one outlet tubing port to which the respective holes led. The Liquid Cell B had each hole leading to an individual tubing port. The inlet/outlet hole arrangements of Liquid Cell A and Liquid Cell B are shown in Figs. 5.2 and 5.3, respectively.

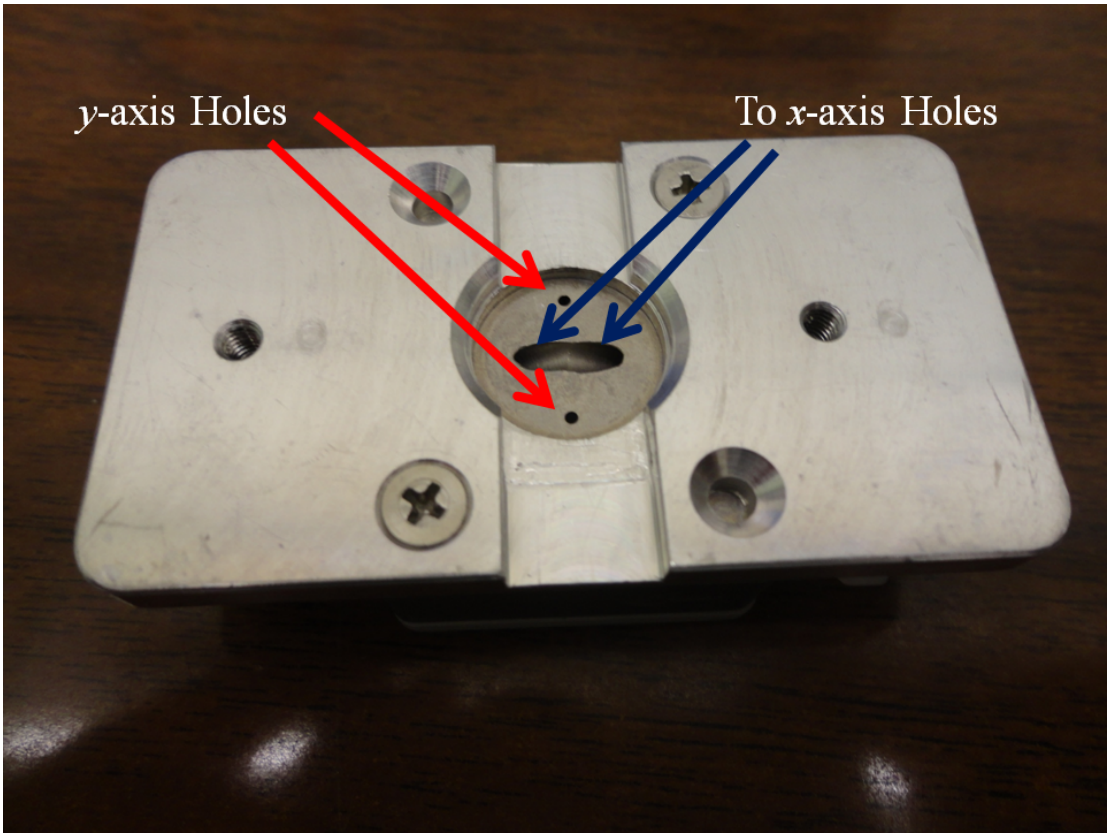

Figure 5.1: Photograph of a liquid cell lid. The two vertically aligned holes on the y-axis are directly on top of the quartz crystal when the liquid cell is assembled. The horizontally aligned holes are where the beam channel for the ellipsometry probing light meets the windows.

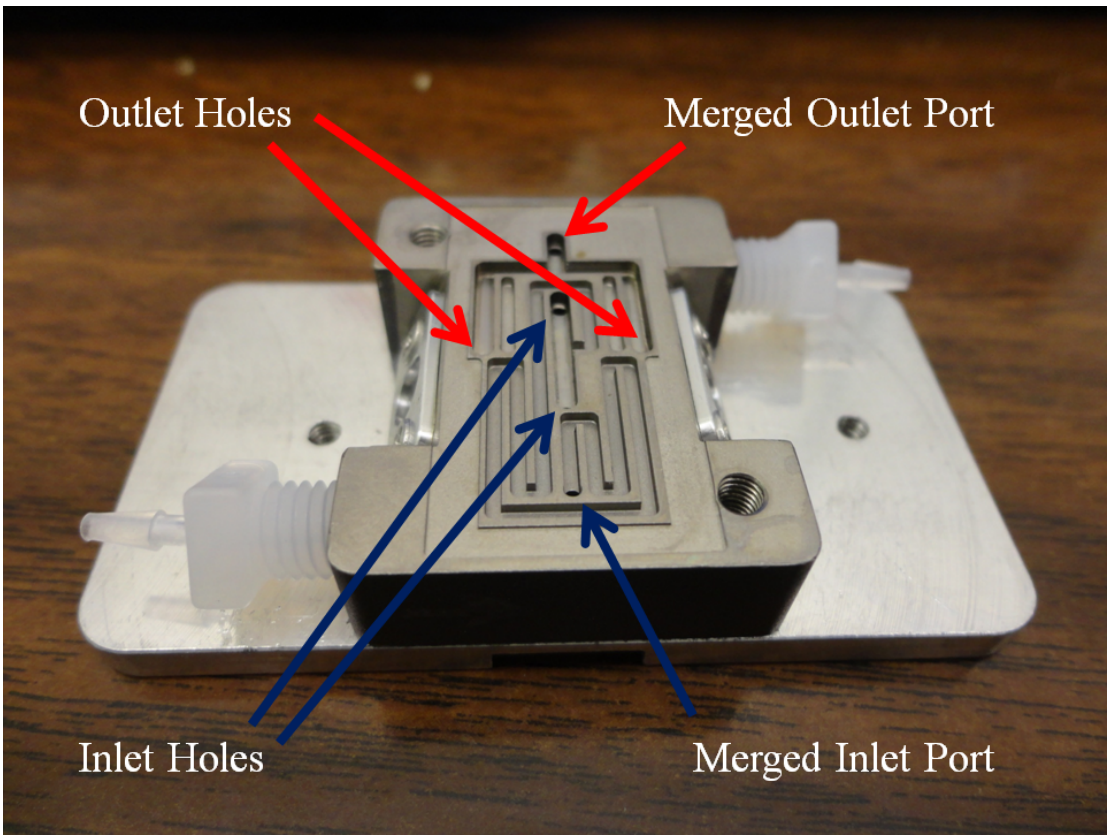

Figure 5.2: Arrangement of inlet/outlet holes and ports for Liquid Cell A.

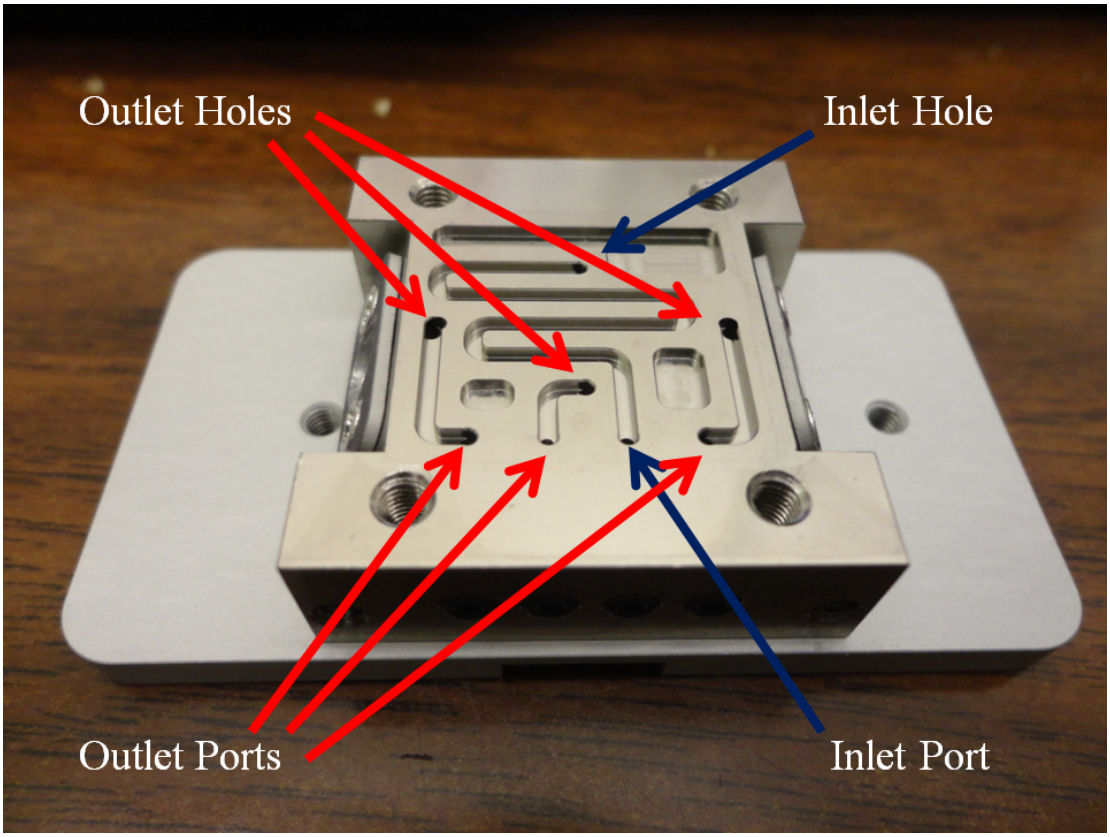

Figure 5.3: Arrangement of inlet/outlet holes and ports for Liquid Cell B.

The single-rinse 2.5 mM CTAB experiment occurred within Liquid Cell A, and the double-rinse 2.5 mM CTAB experiment occurred within Liquid Cell B. A syringe pump (NE-500, New Era Pump Systems, Farmingdale, NY) was used to pull solution through Liquid Cell A. On the other hand, a peristaltic pump (IPC-N 8, IDEX Health & Science, Oak Harbor, WA) was used for Liquid Cell B. As shown in Fig. 5.3 for Liquid Cell B, incoming solution flows along the ellipsometry plane of incidence (x-axis) in each direction to a respective window outlet hole and across the ellipsometry plane of incidence to the final outlet hole. On the other hand, Liquid Cell A will ideally have solution flow evenly along the ellipsometry plane of incidence to the outlet holes over the windows; however, because the outlet holes share one outlet port that leads to the drain pump, the flow rates within the liquid cell to each outlet hole are not necessarily identical.

CompleteEASE® allows the recording of light beam alignment during dynamic measurements. x- and y-axis alignment data are shown d_{SE} plots for the 2.5 mM CTAB experiments in Figs. 5.4 and 5.5, respectively. When CTAB solution or a water rinse enters the liquid cell, one can see that the alignment parameters deviate and return to their original baselines. Furthermore, the directions of the alignment perturbations are generally opposite for CTAB introduction as compared to water rinse introduction. These results imply that CTAB is introduced into the liquid cell asymmetrically. The surfactant film first forms at the entry-favored side. When the water rinse is introduced into the liquid cell, the surfactant film is first removed at that same side. At the end of the adsorption/rinsing process, the film is completely formed/removed, and the alignment parameters return to their baseline values. These observations, coupled with the double-rinse 2.5 mM CTAB experimental result that a faster pump speed results in faster film formation, demonstrate that the experimental setup is diffusion-limiting for CTAB adsorption and rinsing kinetics. Therefore, care must be taken when evaluating adsorption and desorption kinetics with the experimental setup.

An important observation is that features (*e.g.*, minima or maxima) of the SE thickness and alignment parameters usually coincide with time. For both Figs. 5.4 and 5.5, the x-axis parameter has a stronger relationship with the thickness parameter. It is suggested here that this effect is related to liquid flow asymmetry

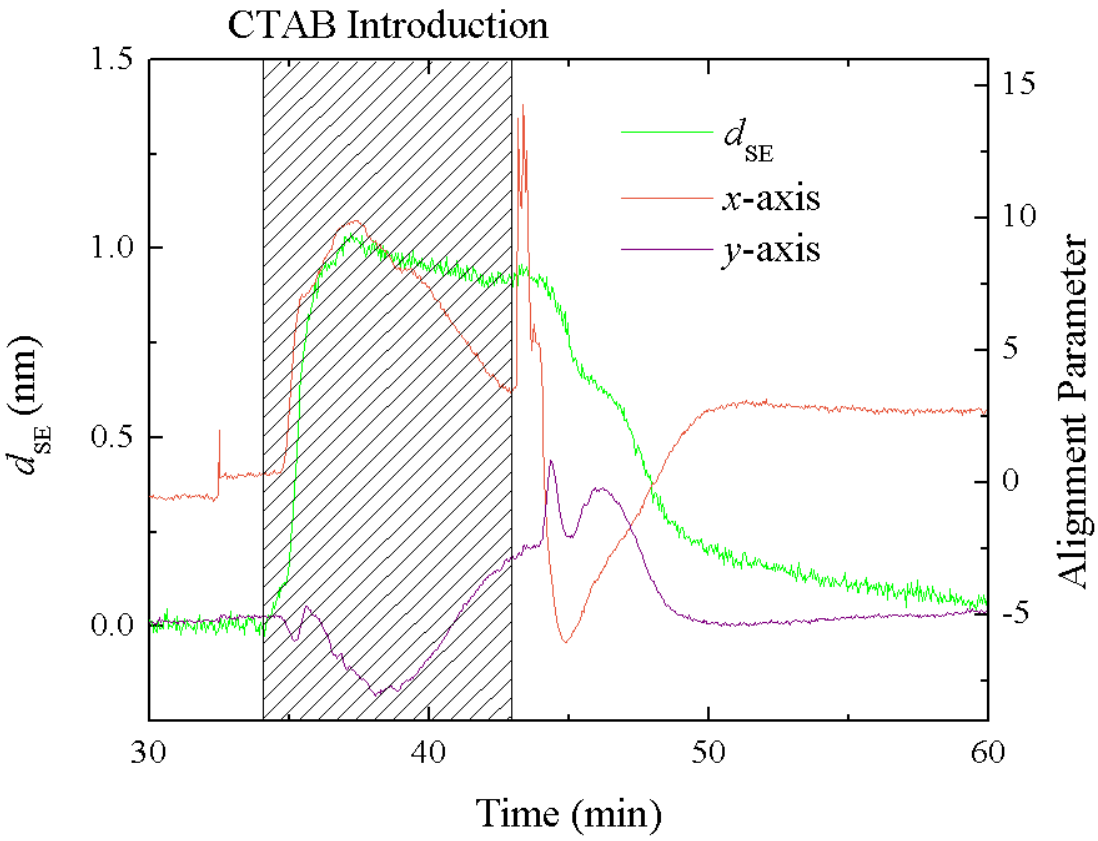

Figure 5.4: d_{SE} and alignment parameters for the single-rinse 2.5 mM CTAB experiment. The graph is shaded when CTAB is directed into Liquid Cell A. Note that features in d_{SE} and x-axis alignment parameters tend to coincide.

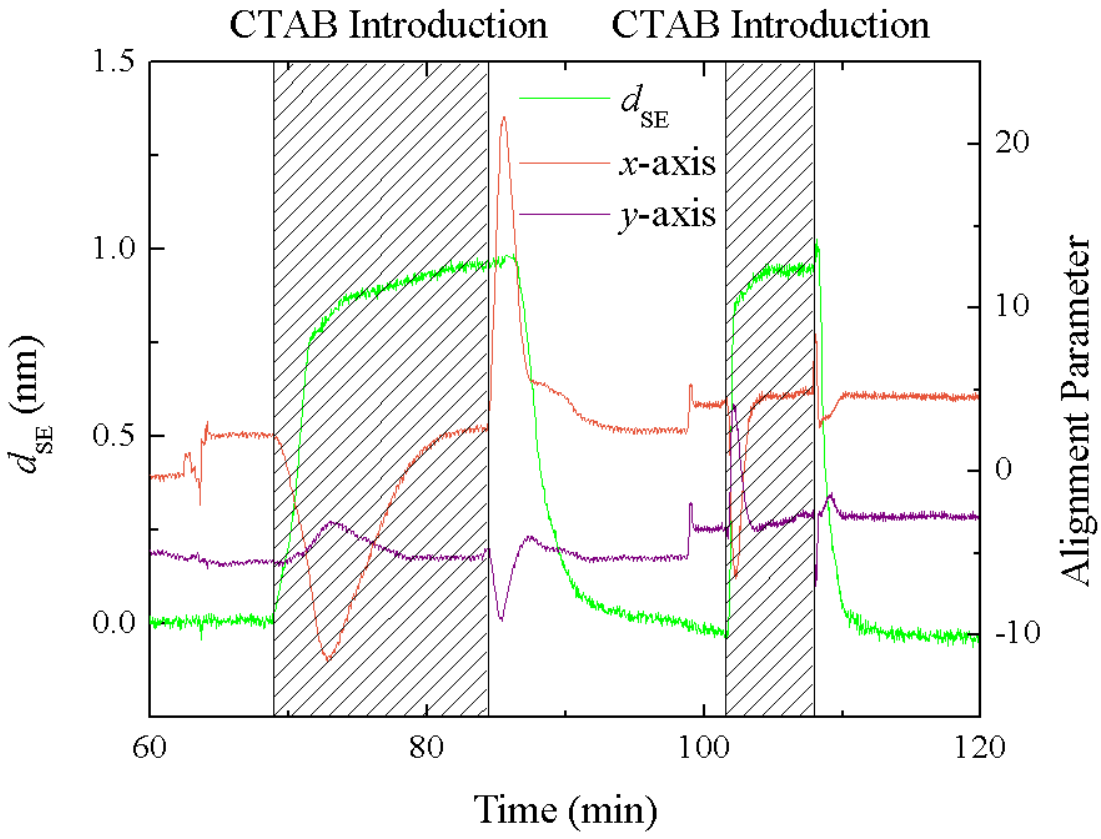

Figure 5.5: d_{SE} and alignment parameters for the double-rinse 2.5 mM CTAB experiment. The graph is shaded when CTAB is directed into Liquid Cell B. Note that features in d_{SE} and x-axis alignment parameters tend to coincide.

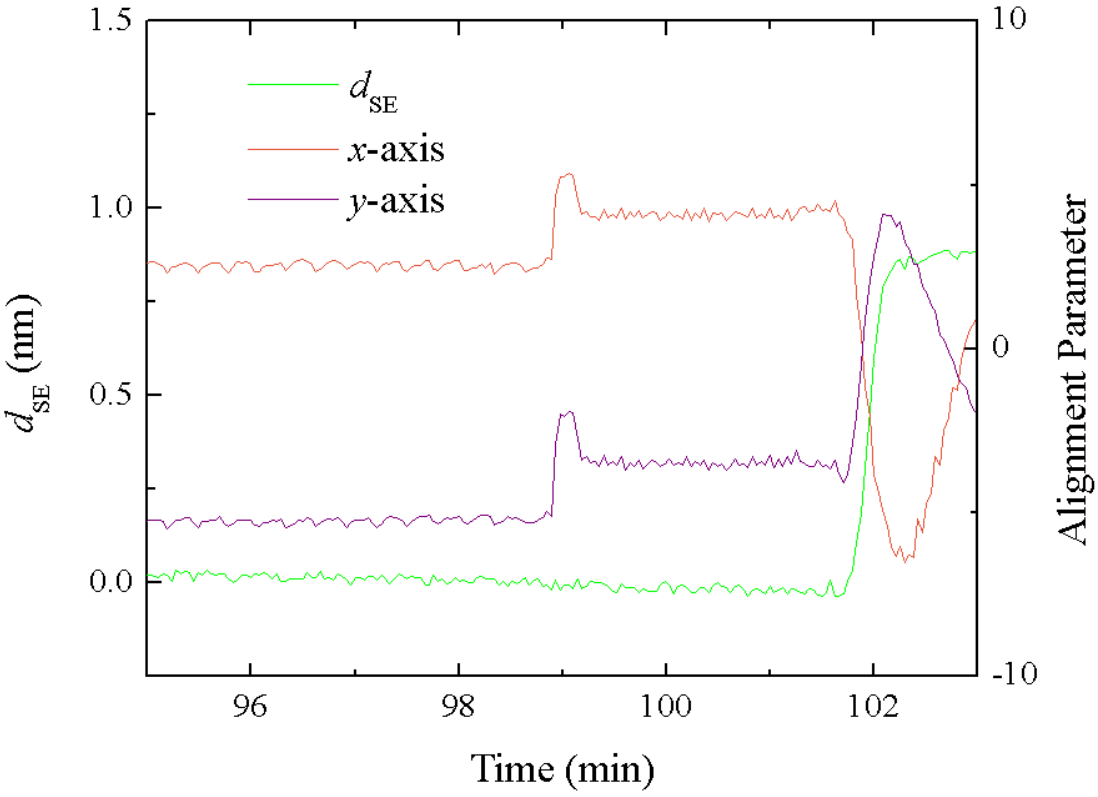

Figure 5.6: Close view of d_{SE} and alignment parameters for the double-rinse 2.5 mM CTAB experiment before and after the pump speed is increased from 0.1 $\frac{\text{mL}}{\text{min}}$ to 0.5 $\frac{\text{mL}}{\text{min}}$ at $t = 99$ min.

and that flow for both liquid cells is more uneven across the liquid cell x-axis (ellipsometry plane of incidence). In Fig. 5.4, CTAB introduction and removal are associated with x-axis alignment parameter maxima and minima, respectively; in Fig. 5.5, CTAB introduction and removal are associated with x-axis alignment parameter minima and maxima, respectively. Again, whether the x-axis alignment parameter goes through a maxima or minima is hypothesized to be related to the side of the liquid cell that favors liquid introduction. As shown in Fig. 4.4, the SE and QCM thickness parameters have parallel features; because these two instruments operate under completely different measurement principles, the SE thickness parameter features in Figs. 4.4 and 5.4 are not likely data artifacts. Rather, the differences between the thickness parameter features of single-rinse and double-rinse 2.5 mM CTAB experiments may be due to variations of liquid flow effects.

Additionally, for the double-rinse 2.5 mM CTAB experiment, one can observe oscillations in the alignment parameters. When the pump speed is increased at $t = 99$ min, the oscillation frequencies increase, as shown by Fig. 5.6. These features are seen in parallel by the QCM-D, but the SE thickness parameter is not significantly affected by the change in pump speed.

Because QCM-D is a mechanical technique where the sensor is in continuous contact with the ambient medium, the instrument is sensitive to perturbations in liquid flow. Careful observation of the QCM thickness parameter (linear with respect to the frequency raw data) for the double-rinse 2.5 mM CTAB experiment reveals highly oscillatory background noise. In similar fashion to the SE alignment parameters, the QCM thickness parameter oscillation frequency and amplitude are shown by Fig. 5.7 to increase with pump speed. In this case, the author hypothesizes that the oscillations are related to the rotation speed of the peristaltic pump rollers and that the peristaltic tubing has degraded in quality, no longer allowing for steady, uniform fluid flow. From the QCM-D perspective, the oscillatory data artifacts are less important for large molecule adsorption with total adsorption frequency change on the order of 100 Hz or greater. However, for organic films on the order of 10 nm or less that can have total adsorption

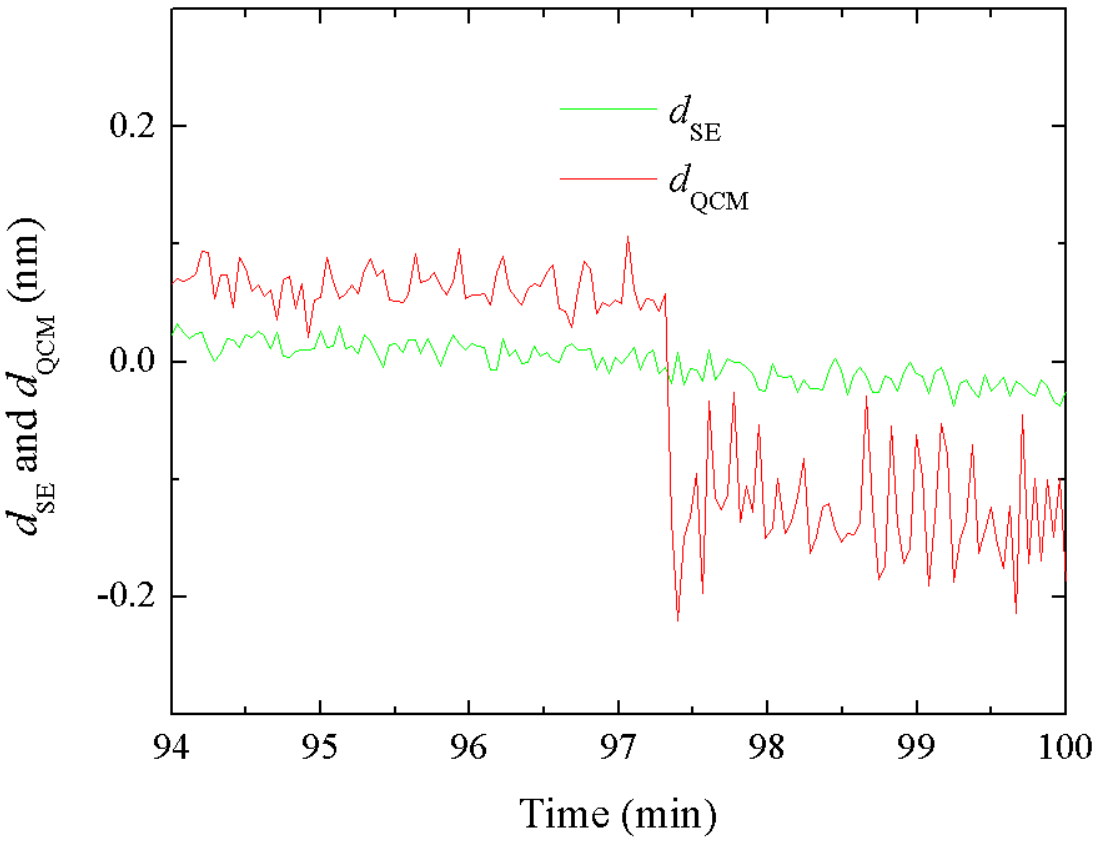

Figure 5.7: SE and QCM thickness parameters for the double-rinse 2.5 mM CTAB experiment, before and after the pump speed is increased from 0.1 $\frac{\text{mL}}{\text{min}}$ to 0.5 $\frac{\text{mL}}{\text{min}}$ at $t = 99$ min.

frequency changes on the order of 10 Hz or less, liquid flow related artifacts have an impact on data quality that should be considered.

5.1.2 QCM-D stability

The stability of QCM-D frequency and dissipation signals is of particular importance for films with total adsorption frequency changes on the order of 10 Hz or less. A QCM-D frequency drift as low as 0.5 $\frac{\text{Hz}}{\text{hr}}$ can have a substantial effect on data during a 30 min adsorption time. Achieving a lower QCM-D drift during experiments can be a challenge, but linear or exponential regressions of non-zero

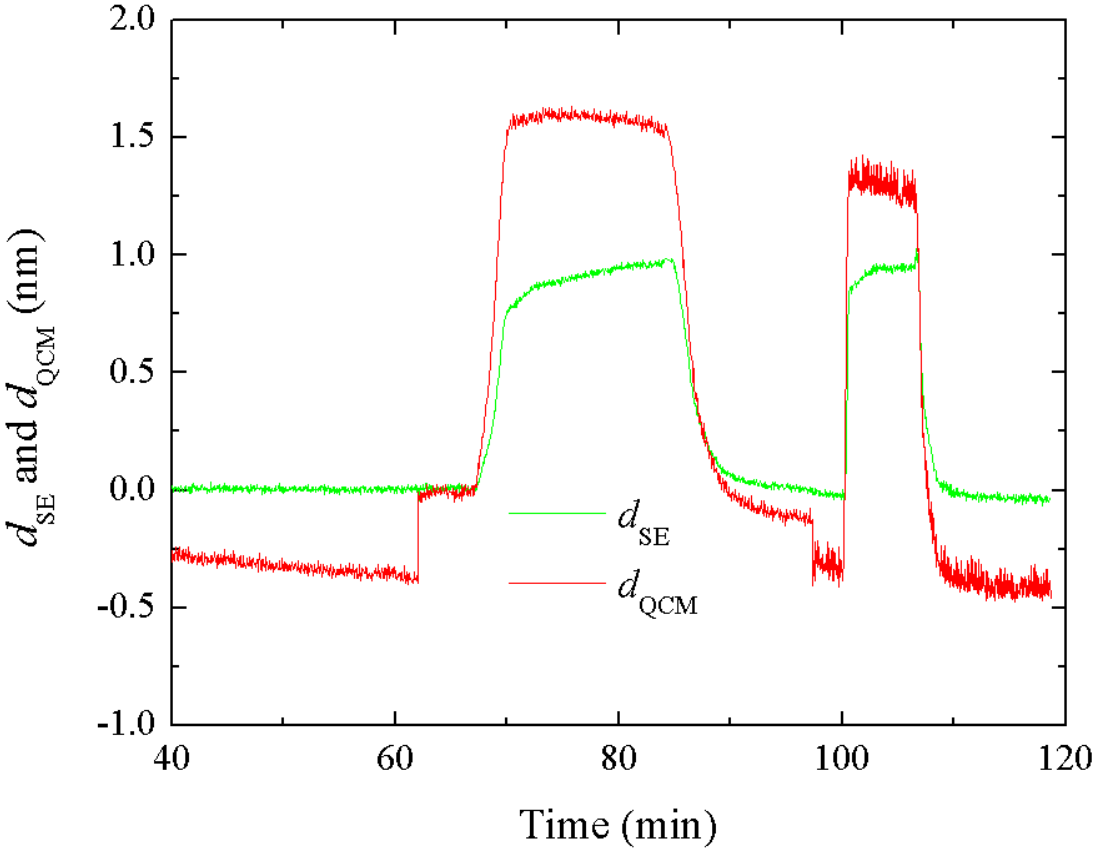

Figure 5.8: Thickness parameters before QCM-D drift correction.

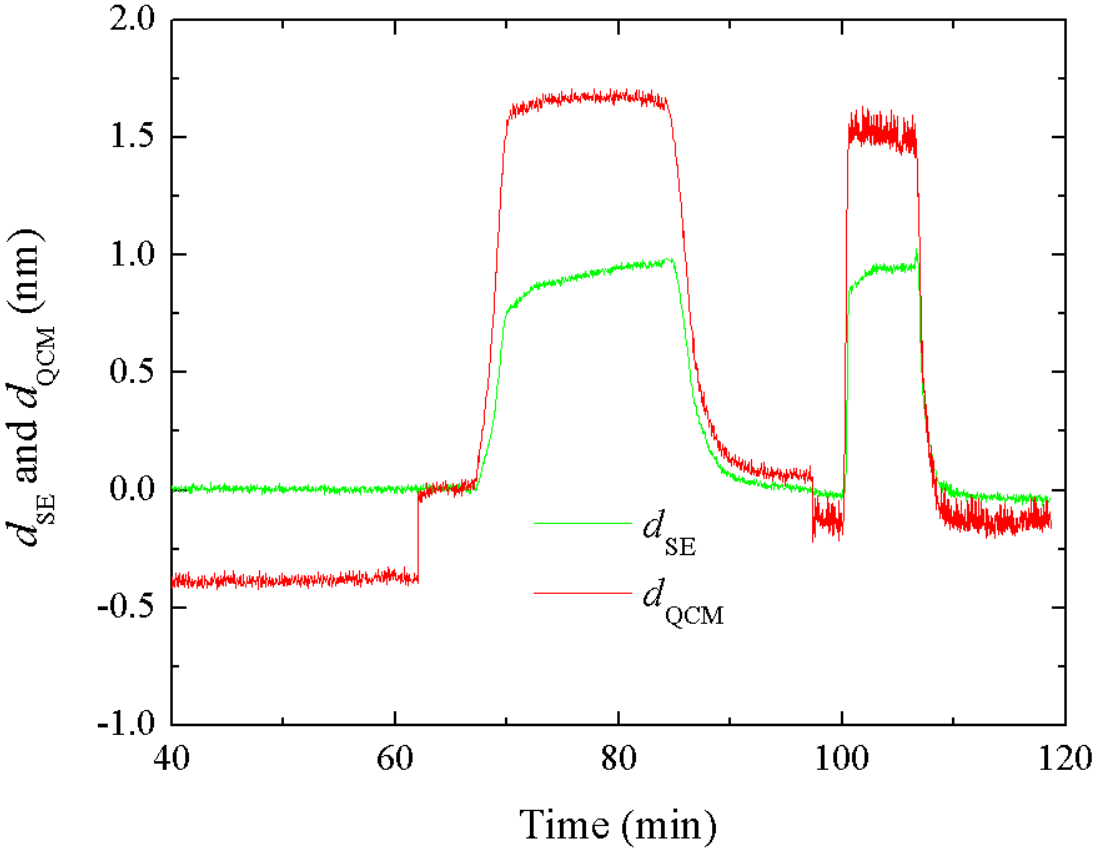

Figure 5.9: Thickness parameters after QCM-D drift correction.

QCM-D baselines prior to film adsorption can be calculated and extrapolated over the entire adsorption process. Fig. 5.8 shows d_{SE} and d_{QCM} for the double-rinse 2.5 mM. Note that the d_{QCM} baseline is decreasing. By determining a linear regression for the d_{QCM} baseline data and compensating for the drift over the entire measurement, Fig. 5.9 can be achieved. The QCM data more closely mirrors the SE data after this correction.

The step changes in d_{QCM} ($t = 62$ min and $t = 99$ min) for Figs. 5.8 and 5.9 are related to perturbations that can be caused by switching the valve or adjusting the pump flow. By offsetting the d_{QCM} data to negate these step changes, one can obtain Fig. 4.5.

5.2 Surfactant adsorption and rinsing

5.2.1 0.1 mM CTAB adsorption and rinsing

The 0.1 mM CTAB adsorption presents a simple case where the film structure does not change during the experiment. The adsorption and desorption processes are both simple, and $f_o^{\mathrm{m,V}}$ is uniform throughout attachment and rinsing. These observations indicate that the CTAB molecules assemble in flat patches of uniform density within the patches, where growth or rinsing occurs by adding or removing molecules at the boundaries of the patches. The slight decrease of the adsorbate fraction during rinsing could be attributed to water displacing individual CTAB molecules within the still-cohesive film patches. The number or size of individual patches (*i.e.*, lateral resolution) is indeterminable by the SE/QCM technique. Similar measurements by SE/QCM could be used to determine adsorption isotherms.[49]

5.2.2 2.5 mM CTAB adsorption and rinsing

Velegol *et al.*[50] studied CTAB adsorption from micellar solutions on silica and concluded from AFM investigations that the surfactants form rodlike structures. Recent AFM studies on CTAB adsorption on gold surfaces indicated rodlike structures, where rough surfaces revealed hemicylindrial and hemispherical shapes.[51]

Shi *et al.*[52] studied adsorption isotherms of CTAB on gold surfaces by QCM-D and AFM and concluded that CTAB formed a patchy cylindrical structure. Macakova, Blomberg, and Claesson concluded from optical reflectometry, QCM-D, and AFM studies that CTAB adsorbs in the form of micelles that look like rods with their projected shape along silica surfaces.[9]

The conclusions of Macakova, Blomberg, and Claesson were supported by the optically obtained surface density $\Gamma_{\mathrm{REF}} = 1.90\,\frac{\mathrm{mg}}{\mathrm{mL}}$ from reflectometry, denoted by the subscript, and the larger mechanically obtained surface density $\Gamma_{\mathrm{QCM}} = 2.7\,\frac{\mathrm{mg}}{\mathrm{m}^2}$ from QCM-D; the difference between the surface density parameters was attributed to water content within the adsorbed layer. The ratio $(\Gamma_{\mathrm{QCM}} - \Gamma_{\mathrm{REF}})/\Gamma_{\mathrm{REF}} = 0.42$ was used to characterize the topology of the adsorbed surfactants and indicated short rods or combinations of rods and spherical micelles.[9] This ratio is very close to the ratio found here for the single-rinse 2.5 mM CTAB measurement ($\Gamma_{\mathrm{SE}} = 0.82\,\frac{\mathrm{mg}}{\mathrm{m}^2}$ and $\Gamma_{\mathrm{QCM}} = 1.17\,\frac{\mathrm{mg}}{\mathrm{m}^2}$, [Fig. 4.4 at $t = 20$ min]): $(\Gamma_{\mathrm{QCM}} - \Gamma_{\mathrm{SE}})/\Gamma_{\mathrm{SE}} = 0.43$, suggesting that CTAB adsorbed on gold from 2.5 mM solution forms a similar topography.

However, the surface density of CTAB adsorbed onto gold of this study is lower by more than a factor of 2 compared with silica. The surface density of CTAB on gold reported by Shi *et al.*,[52] $\Gamma_{\mathrm{QCM}} = 1.9\pm\ 0.4\,\frac{\mathrm{mg}}{\mathrm{m}^2}$ when approaching 1.32 mM CTAB concentration, is also smaller than that of Macakova, Blomberg, and Claesson but still greater than the surface density reported here. These observations are consistent with the commonly attributed larger negative surface charge on silica than gold. From comparison with these previous reports, one can therefore conclude that 2.5 mM CTAB on Au forms topographies (a) with regions of rodlike and spherelike bilayer structures and (b) with lower overall surface coverage than on silica.

5.3 Observation of alkanethiol SAM chemisorption

SAM chemisorption from solution is generally considered a two-step process.[53] The first step consists of adsorbate molecules attaching to the surface in random orientations as the substrate surface permits. Over time the attached molecules change conformation and make room for new molecules to chemisorb into patches around initial nucleation sites. The initial SAM patches grow and reorganize so they eventually merge to form a polycrystalline structure. Typically the initial attachment step is comparatively short and encompasses most of the total chemisorption. On the other hand, the second, reorganization step typically is longer and contributes less material to the SAM.

Jakubowicz *et al.* used the following techniques, *ex-situ*, to characterize octadecanethiol and *p*-nitrobenzenethiol SAM growth on Au: single-wavelength ellipsometry, contact angle measurements, parallel angle-resolved X-ray photoelectron spectroscopy (ARXPS), and Fourier transform infrared (FTIR) spectroscopy. The authors described the SAM growth in terms of Langmuir isotherm kinetics and concluded that SAM growth consisted of a faster initial growth phase and a slower "saturation" phase. Jakubowicz *et al.* also found that SAMs formed from dilute thiol solutions exhibited a specific behavior at the beginning of the initial growth phase where adsorbate molecules tended to take a conformation flat across the substrate. The authors did not have sufficient time resolution with their *ex-situ* instrumentation to explicitly notice the briefer flat conformation of more concentrated thiol solutions.[53]

The results shown in Fig. 4.7 reinforce the idea of a two-step process. The transition between the growth and reorganization steps can be seen at $t = 150\,\mathrm{min}$. $f_{\mathrm{o}}^{\mathrm{V}}$ is uniform throughout the measurement, implying that the porosity is consistent throughout the ultra-thin film growth.

Because SAMs are thought to be well-packed, the low adsorbate fraction parameter may seem inaccurate. The effect of solvent on SAM formation and quality is important but still not entirely understood, though ethanol is the most widely used solvent for preparing SAMs from solution.[39] Water is more polar than

ethanol and does not solvate alkanethiols or their derivatives as well as ethanol. Thus, the use of water as a solvent could cause SAM defects, resulting in a rougher surface and larger contact area with water. A larger interfacial area between the adsorbate layer and ambient would allow more solvent molecules to mechanically couple with the adsorbate and contribute to the d_{QCM} parameter, simultaneously causing $f_{\mathrm{o}}^{\mathrm{V}}$ to decrease. Because the adsorbate molecules have an alcohol tail group, d_{QCM} may also include water that is mechanically coupled to the organic layer via hydrogen bonds. Though the SE/QCM technique is intended to provide a quantitative measure of the ultra-thin film porosity, care must be taken when one considers where mechanically coupled solvent resides. The combinatorial technique described here cannot distinguish between coupled solvent on top of the organic layer and coupled solvent within the organic layer.

5.4 Evaluation of aptamer-based DNA biosensor

During probe chemisorption in Fig. 4.8, a well-packed layer is formed due to the similarity of the thickness changes reported by SE and QCM. The adsorbate volume fraction remains high upon the introduction of the passivating SAM. Interestingly, d_{SE} decreases during SAM formation, suggesting that large DNA probes are displaced by relatively short SAM molecules. The film retains a high adsorbate volume fraction at this point.

An ideal experiment for evaluating the performance of the aptamer DNA sensor would be to prepare two samples and interrogate one with non-complementary DNA and the second with complementary DNA. However, the example shown in Fig. 4.8, whereby the interrogations occur in sequence on the same sample, is illustrative of how the porosity measurement provided by the combinatorial SE/QCM technique is useful. If only the SE data is considered, one observes that more complementary DNA attaches to the surface than non-complementary DNA, implying that the sensor is selective to complementary DNA. On the other hand, the QCM shows a higher signal for non-complementary DNA than for complementary DNA; a conclusion on selectivity cannot be formed, however, because the influence of bound water on each case cannot be determined.

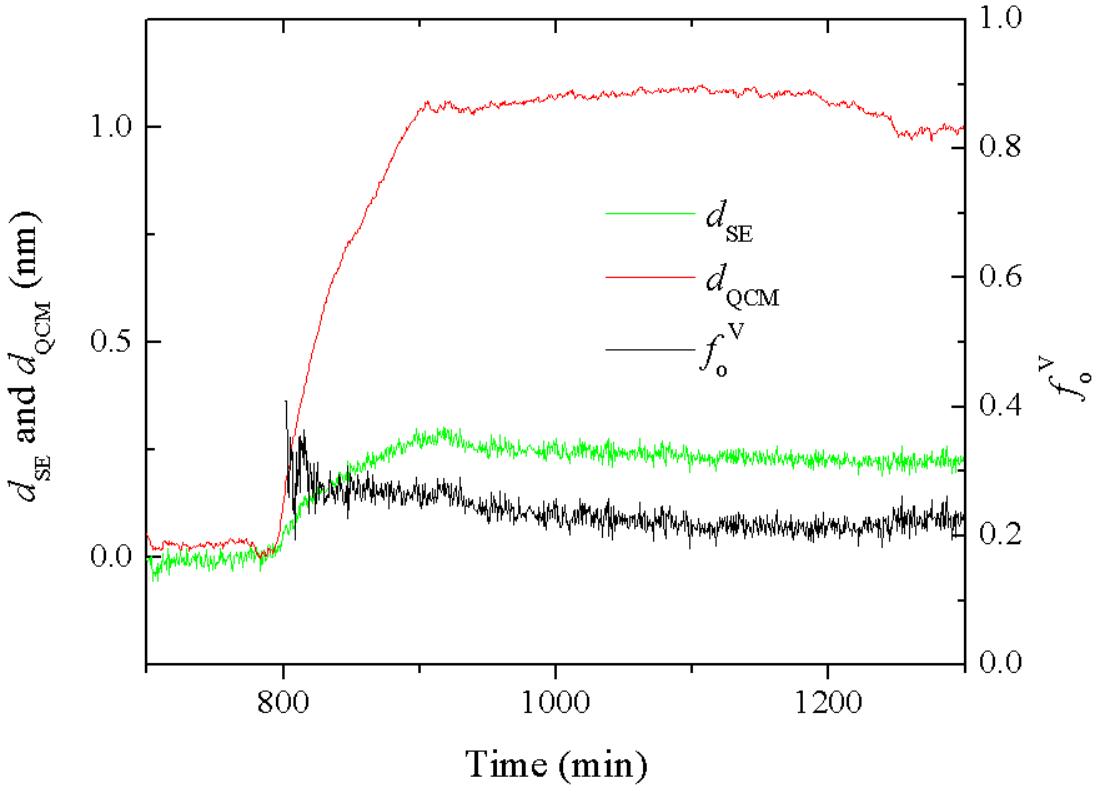

Figure 5.10: Thickness and adsorbate volume fraction parameters for non-complementary DNA interrogation.

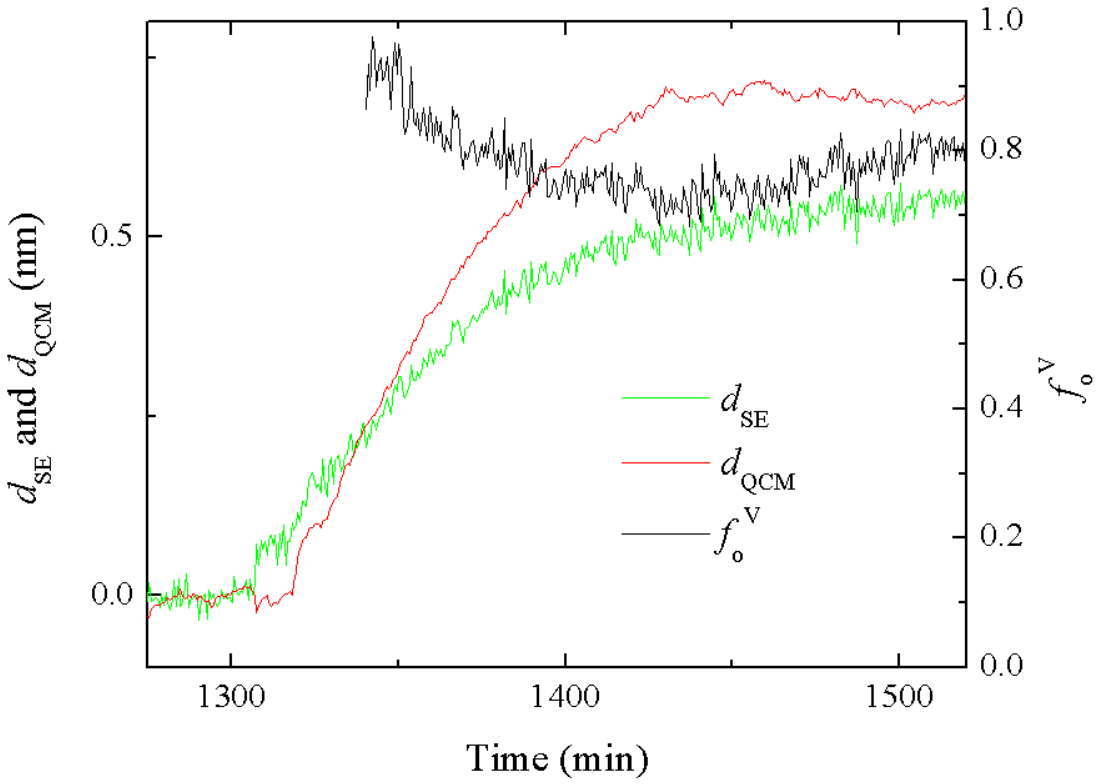

Figure 5.11: Thickness and adsorbate volume fraction parameters for complementary DNA interrogation.

It is through the adsorbate volume fraction parameter that a more comprehensive understanding of the different adsorption scenarios can be developed. Because changes in porosity due to equivalent additions of adsorbate become less noticeable as the total film thickness increases, it can be useful to examine each adsorption step independently. Figs. 5.10 and 5.11 show the thickness and porosity parameters for the non-complementary DNA and complementary DNA adsorption processes, respectively. The adsorbate fraction parameter is much lower in Fig. 5.10 (approximately 0.2) than in Fig. 5.11 (approximately 0.8). These results imply that non-complementary DNA and complementary DNA adsorb to the surface in distinct ways. A hypothesis proposed here is that the non-complementary DNA adsorbs to the surface of the aptamer DNA probe layer and has portions dangling into solution that are highly solvated, reflecting a high porosity (low adsorbate volume fraction parameter). Nucleobases on the non-complementary DNA strand form hydrogen bonds with water molecules instead of absent partner nucleobases. In contrast, the complementary DNA forms a predicted tight hybridized structure with the aptamer DNA probe molecules, and little additional water associates with the hybridized structure.

By using data from both SE and QCM to determine the dynamic adsorbate volume fraction parameter as outlined here, one can distinguish between alternative adsorption mechanisms or judge the binding affinity of an analyte material to a surface probe molecule.

Chapter 6

Conclusions

In conclusion, the author described a combinatorial SE/QCM technique for monitoring the real-time thickness and porosity evolution of rigid, transparent, organic ultra-thin films. The hybrid approach was necessary because neither optical SE nor acoustical QCM can independently distinguish between the thickness and porosity of films that meet the optical ultra-thin film limit $2\pi nd/\lambda \ll 1$. Using a virtual separation approach, the author was able to arbitrarily rearrange the components of heterogeneous, isotropic ultra-thin films from the standpoint of SE. Equations for determining an ultra-thin film's thickness and adsorbate fraction parameters from SE and QCM raw data were derived. Different scenarios of the measured system were considered, depending if the dry adsorbate and liquid ambient densities were equal or not. Data acquisition protocols for use with a multiple-flow inlet control system were introduced. Finally, the application of SE/QCM toward analyzing relevant single- and multiple-layer organic ultra-thin films was discussed.

There are many possible future avenues for research with the combinatorial technique. Protein structure can be an important element of function. Adsorbate fraction parameters for protein layers on top of different SAMs could be compared to verify if the conformation of the proteins is affected by the SAM terminal functional group. The QCM-D responses for organic attachment under water ambient and heavy water (deuterium oxide) ambient could be compared to determine the effect of liquid on frequency and dissipation or gain new information on the location of water bound to the organic layer.

Organic adsorption on three-dimensional spatially coherent (anisotropic) nanostructures could be monitored with generalized ellipsometry (GE) and QCM. The nanostructures would provide an increased surface area for greater organic attachment. Organic attachment would modulate the birefringence of the nanostructures, and GE has been shown to be extremely sensitive to the birefringence of anisotropic materials.

An electrochemistry apparatus could be added to the liquid cell to explore ionic effects. For example, one could probe the electrical double layer that forms at the solid-liquid interface; knowledge of the electrical double layer could help answer the question of where bound liquid is located. Alternatively, the substrate surface potential could be adjusted to promote or deter the adsorption of charged materials.

Appendix A

Abbreviations

AFM: Atomic force microscopy

ARXPS: Angle-resolved X-ray photoelectron spectroscopy

CMC: Critical micelle concentration

CTAB: Cetyltrimethylammonium bromide

DNA: Deoxyribonucleic acid

DPI: Dual polarization interferometry

EQCM: Electrochemical quartz crystal microbalance

FTIR: Fourier transform infrared

GE: Generalized ellipsometry

QCM: Quartz crystal microbalance

QCM-D: Quartz crystal microbalance with dissipation

SAM: Self-assembled monolayer

Appendix B

Definitions

Adsorbate: the material that attaches to a surface via adsorption or chemisorption.

Chemisorption: a specific form of adsorption where the adsorbate forms a chemical bond with the surface.

Critical micelle concentration (CMC): the minimum concentration of surfactant necessary for full micelles to form.

Quartz crystal microbalance (QCM): an acoustical technique that measures the vibration frequency shifts of odd overtones of a quartz crystal that is oscillating in a shear mode. QCM data can be used to determine real-time mechanical property changes of surface layers and ambient fluid.

Quartz crystal microbalance with dissipation (QCM-D): a variant of QCM where the quartz crystal vibrates in pulses. Shifts in the frequency signal decay are also measured and used in the modeling of viscoelastic behavior.

Self-assembled monolayer (SAM): a surface layer formed by chemisorbing molecules that naturally arrange themselves into a uniform structure, usually employed to adjust the surface properties of a material.

Spectroscopic ellipsometry (SE): an optical technique that measures the change in polarization state of light. Optical models are constructed that allow

physical properties of samples to be determined following a procedure of best-matching experimental and model-calculated data.

References

[1] Q. Zhang and V. Subramanian, Biosensors and Bioelectronics **22**, 3182 (2007). 1

[2] S. Sarkar, B. C. Isenberg, E. Hodis, J. B. Leach, T. A. Desai, and J. Y. Wong, Journal of Biomaterials Science-polymer Edition **19**, 1347 (2008). 1

[3] S. C. Howell, R. Mittal, L. J. Huang, B. Travis, R. M. Breyer, and C. R. Sanders, Biochemistry **49**, 9572 (2010). 1

[4] E. Bittrich, K. B. Rodenhausen, K.-J. Eichhorn, T. Hofmann, M. Schubert, M. Stamm, and P. Uhlmann, Biointerphases **5**, 1 (2010). 1

[5] A. Domack, O. Prucker, J. Rühe, and D. Johannsmann, Phys. Rev. E **56**, 680 (1997). 2, 3

[6] J. J. R. Stålgren, J. Eriksson, and K. Boschkova, J. Colloid Interf. Sci. **253**, 190 (2002). 2

[7] M. J. Swann, L. L. Peel, S. Carrington, and N. J. Freeman, Analytical Biochemistry **329**, 190 (2004).

[8] R. P. Richter and A. R. Brisson, Biophys. J. **88**, 3422 (2005). 2, 3

[9] L. Macakova, E. Blomberg, and P. M. Claesson, Langmuir **23**, 12436 (2007). 2, 3, 52

[10] C. Aulin, I. Varga, P. M. Claesson, L. Wagberg, and T. Lindstrom, Langmuir **24**, 2509 (2008). 2

[11] L. Broch, L. Johann, N. Stein, A. Zimmer, and R. Beck, Rev. Sci. Instrum. **78**, 064101 (2007). 3

[12] K. B. Rodenhausen, T. Kasputis, A. K. Pannier, J. Y. Gerasimov, R. Y. Lai, M. Solinsky, T. E. Tiwald, A. Sarkar, T. Hofmann, N. Ianno, et al., Rev. Sci. Instrum. **82**, 103111 (2011). 3

[13] K. B. Rodenhausen and M. Schubert, Thin Solid Films **519**, 2772 (2011). 3, 13

[14] R. M. Azzam and N. M. Bashara, *Ellipsometry and Polarized Light* (North-Holland Publ. Co., Amsterdam, 1984). 5, 7, 8

[15] H. G. Tompkins and E. A. Irene, eds., *Handbook of Ellipsometry* (William Andrew Publishing, Highland Mills, 2004).

[16] P. Drude, Ann. Phys. **34**, 489 (1888). 5, 13, 16

[17] D. Schmidt, E. Schubert, and M. Schubert, phys. stat. sol. (a) **205**, 748 (2008). 7

[18] G. E. Jellison, Thin Solid Films **313-314**, 33 (1998). 8, 13

[19] G. E. Jellison, in *Handbook of Ellipsometry*, edited by E. A. Irene and H. W. Tompkins (William Andrew Publishing, 2004). 13

[20] H. Fujiwara, *Spectroscopic Ellipsometry* (John Wiley & Sons, New York, 2007). 8

[21] D. E. Aspnes and A. A. Studna, Phys. Rev. B **27**, 985 (1983). 8, 16

[22] D. E. Aspnes, in *Handbook of Optical Constants of Solids*, edited by E. D. Palik (Academic Press, New York, 1998), vol. I, p. 89.

[23] A. Röseler, *Infrared Spectroscopic Ellipsometry* (Akademie-Verlag, Berlin, 1990). 8

[24] T. Berlind, G. K. Pribil, D. Thompson, J. A. Woollam, and H. Arwin, phys. stat. sol. (c) **5**, 1249 (2008). 8

[25] I. Abdulhalim, L. Benguigui, and R. Weil, J. Phys.-Paris **46**, 815 (1985). 8

[26] M. Schubert, in *Introduction to Complex Mediums for Optics and Electromagnetics*, edited by W. S. Weiglhofer and A. Lakhtakia (SPIE, Bellingham, WA, 2004), pp. 677 – 710.

[27] M. Schubert, Phys. Rev. B **53**, 4265 (1996).

[28] M. Schubert, *Infrared Ellipsometry on semiconductor layer structures: Phonons, plasmons and polaritons*, vol. 209 of *Springer Tracts in Modern Physics* (Springer, Berlin, 2004). 8

[29] F. Höök, M. Rodahl, P. Brzezinski, and B. Kasemo, Langmuir **14**, 729 (1998). 13

[30] G. Sauerbrey, Z. Phys. A-Hadron Nucl. **155**, 206 (1959). 14

[31] M. Rodahl, F. Höök, C. Fredriksson, C. A. Keller, A. Krozer, P. Brzezinski, M. Voinova, and B. Kasemo, Faraday Discuss. **107**, 229 (1997). 14

[32] K. B. Rodenhausen, M. Guericke, A. Sarkar, T. Hofmann, N. Ianno, M. Schubert, T. E. Tiwald, M. Solinsky, and M. Wagner, Thin Solid Films **519**, 2821 (2011). 16

[33] M. Schubert, Ann. Phys. **15**, 480 (2006). 16

[34] N. V. Edwards, M. D. Bremser, T. W. Weeks, Jr., R. S. Kern, R. F. Davis, and D. E. Aspnes, Appl. Phys. Lett. **69**, 2065 (1996). 16

[35] B. Johs and J. S. Hale, Phys. Status Solidi A **205**, 715 (2008). 16

[36] L. Sepulveda and J. Cortes, J. Phys. Chem.-US **89**, 5322 (1985). 26

[37] G. Wei, L. Wang, H. Zhou, Z. Liu, Y. Song, and Z. Li, Appl. Surf. Sci. **252**, 1189 (2005). 26

[38] F. van Ruissen, M. Le, J. M. Carroll, P. G. M. van der Valk, and J. Schalkwijk, J. Invest. Dermatol. **110**, 358 (1998). 26

[39] J. C. Love, L. A. Estroff, J. K. Kriebel, R. G. Nuzzo, and G. M. Whitesides, Chem. Rev. **105**, 1103 (2005). 34, 53

[40] K. B. Rodenhausen, B. A. Duensing, T. Kasputis, A. K. Pannier, T. Hofmann, M. Schubert, T. E. Tiwald, M. Solinsky, and M. Wagner, Thin Solid Films **519**, 2817 (2011). 34

[41] C. Fan, K. W. Plaxco, and A. J. Heeger, P. Natl. Acad. Sci. USA **100**, 9134 (2003). 36

[42] X. Zuo, S. Song, J. Zhang, D. Pan, L. Wang, and C. Fan, J. Am. Chem. Soc. **129**, 1042 (2007). 36

[43] C. A. Savran, S. M. Knudsen, A. D. Ellington, and S. R. Manalis, Anal. Chem. **76**, 3194 (2004). 36

[44] J. S. Shumaker-Parry, R. Aebersold, and C. T. Campbell, Anal. Chem. **76**, 2071 (2004). 36

[45] W. Yang, J. Y. Gerasimov, and R. Y. Lai, Chem. Commun. pp. 2902–2904 (2009). 36

[46] 0.33 μM HS-$(CH_2)_6$-5'-CCGTTACGCCACCAGCTCCAAACGG-3'-$(CH_2)_7$-NH-MB. Since the probe was purchased as a disulfide with 1-mercapto-6-hexanol, 200 μM stock probe solution was treated with tris(2-carboxyethyl)phosphine for 1 hr to reduce disulfide bonds. 36

[47] 1 μM 17-base BRCA2 gene segment (5'-TGTACTTCAGGGCCGTA-3'). 36

[48] 1 μM 17-base *K-ras* gene segment (5'-TTGGAGCTGGTGGCGTA-3'). 36

[49] R. A. May, D. W. Flaherty, C. B. Mullins, and K. J. Stevenson, J. Phys. Chem. Lett. **1**, 1264 (2010). 51

[50] S. B. Velegol, B. D. Fleming, S. Biggs, E. J. Wanless, and R. D. Tilton, Langmuir **16**, 2548 (2000). 51

[51] H. C. Schniepp, H. C. Shum, D. A. Saville, and I. A. Aksay, J. Phys. Chem. C **112**, 14902 (2008). 51

[52] L. Shi, M. Ghezzi, G. Caminati, P. Lo Nostro, B. P. Grady, and A. Striolo, Langmuir **25**, 5536 (2009). 52

[53] A. Jakubowicz, H. Jia, R. M. Wallace, and B. E. Gnade, Langmuir **21**, 950 (2005). 53